Search for squarks and gluinos in events with an isolated lepton, jets and missing transverse momentum at $\sqrt{s}$ = 13 TeV with the ATLAS detector

The ATLAS Collaboration

Abstract

The results of a search for squarks and gluinos in final states with an isolated electron or muon, multiple jets and large missing transverse momentum using proton–proton collision data at a centre-of-mass energy of $\sqrt{s}$ = 13 TeV are presented. The dataset used was recorded in 2015 and 2016 by the ATLAS experiment at the Large Hadron Collider and corresponds to an integrated luminosity of 14.8 fb^{-1}.

1 Introduction

Supersymmetry (SUSY) [1–6] is a theoretical framework of physics beyond the Standard Model (SM) that predicts for each SM particle the existence of a supersymmetric partner differing by half a unit of spin. The partner particles of the SM fermions (quarks and leptons) are the scalar squarks ($\tilde{q}$) and sleptons ($\tilde{\ell}$). In the boson sector, the supersymmetric partner of the gluon is the fermionic gluino ($\tilde{g}$), whereas the supersymmetric partners of the Higgs (higgsinos) and the electro-weak gauge bosons (winos and bino) mix to form charged mass eigenstates (charginos) and neutral mass eigenstates (neutralinos). In the minimal supersymmetric extension of the Standard Model (MSSM) [7, 8] two scalar Higgs doublets along with their higgsino partners are necessary, resulting in two charginos ($\tilde{\chi}^{\pm}_{1,2}$) and four neutralinos ($\tilde{\chi}^0_{1,2,3,4}$). SUSY addresses the SM hierarchy problem [9–12] provided that the masses of at least some of the supersymmetric particles (most notably the higgsinos, the top squarks and the gluinos) are near the TeV scale.

In R-parity-conserving SUSY [13], gluinos or squarks might be pair-produced at the Large Hadron Collider (LHC) via the strong interaction and decay either directly or via intermediate states to the lightest supersymmetric particle (LSP). The LSP is stable and is assumed to be only weakly interacting, making it a candidate for dark matter [14, 15].

This note considers SUSY simplified models [16–18] in which pair-produced gluinos or squarks decay via the lightest chargino ($\tilde{\chi}^{\pm}_1$) to the LSP, which is assumed to be the lightest neutralino ($\tilde{\chi}^0_1$). The decay topologies are illustrated in Figure 1. In the squark-production model, the squark decays to the chargino via $\tilde{q} \rightarrow q'\tilde{\chi}^{\pm}_1$. The chargino further decays to the LSP by emitting an on- or off-shell W boson, $\tilde{\chi}^{\mp}_1 \rightarrow W^{(*)\pm}\tilde{\chi}^0_1$, depending on the available phase space. In the gluino-production model, the gluino decays to the lightest chargino and two SM quarks via $\tilde{g} \rightarrow q\bar{q}'\tilde{\chi}^{\pm}_1$, followed by the same chargino decay. This scenario occurs in the MSSM when the gluino decays to a virtual squark and a SM quark, with the squark being the partner particle of the left-handed SM quark. The squark subsequently decays to a SM quark and a chargino with a dominant wino component.
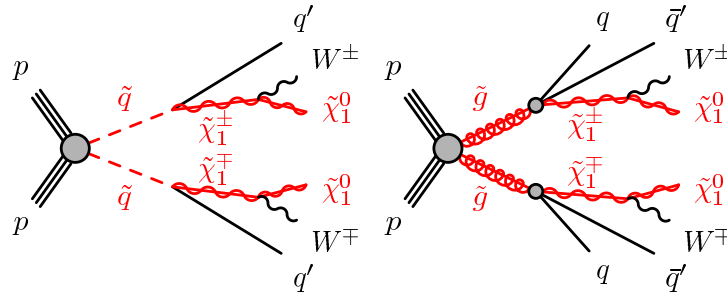

Figure 1: The decay topologies of the signal model considered in this search: squark pair production (left) and gluino pair production (right).

The experimental signature characterising this search consists of a lepton (electron or muon) from the decay of one of the W bosons, several jets, and missing transverse momentum ($E_{\mathrm{T}}^{\mathrm{miss}}$) from the undetectable neutralinos and neutrino(s). The number of detectable leptons and jets and their kinematics depend on the mass and the identity (gluinos or squarks) of the pair-produced sparticles as well as on the masses of the lightest chargino and the neutralino. Ten sets of signal selection criteria, or signal regions (SRs), are defined in order to provide sensitivity to a broad range of mass spectra in both models. In each SR,

the event yield is compared against the expectation from the SM processes, which is estimated using a combination of simulation and observed data in control regions (CRs). The search uses the ATLAS data collected in proton–proton collisions at the LHC in 2015 and 2016 at a centre-of-mass energy of 13 TeV, corresponding to an integrated luminosity of 14.8 fb^{-1}.

The analysis extends previous ATLAS searches with similar event selections performed with data collected in 2010–2012 (LHC Run 1) [19] and in 2015 (Run 2) [20], at centre-of-mass energies of 7–8 TeV and 13 TeV, respectively. The results of all Run 1 ATLAS searches targeting squark and gluino pair-production are summarised in Ref. [21]. The CMS Collaboration has performed similar searches for gluinos decaying via intermediate supersymmetric particles in Run 1 [22, 23] and Run 2 [24].

This note is structured as follows. After a brief description of the ATLAS detector in Section 2, the simulated data samples for the background and signal processes used in the analysis as well as the dataset and the trigger strategy are detailed in Section 3. The reconstructed objects and quantities used in the analysis are described in Section 4 and the event selection is presented in Section 5. The background estimation and the systematic uncertainties associated with the expected event yields are discussed in Sections 6 and 7, respectively, while details of the statistical interpretation are given in Section 8. Finally, the results of the analysis are presented in Section 9 and are followed by a conclusion.

2 ATLAS detector

ATLAS [25] is a general-purpose detector with a forward-backward symmetric design that provides almost full solid angle coverage around the interaction point.[1] The main components of ATLAS are the inner detector (ID), which is surrounded by a superconducting solenoid providing a 2 T axial magnetic field, the calorimeter system, and the muon spectrometer (MS), which is immersed in a magnetic field generated by three large superconducting toroidal magnets. The ID provides track reconstruction within $|\eta| < 2.5$, employing pixel detectors close to the beam pipe, silicon microstrip detectors at intermediate radii, and a straw-tube tracker with particle identification capabilities based on transition radiation at radii up to 1080 mm. The innermost pixel detector layer, the insertable B-layer [26], was added during the shutdown between LHC Run 1 and Run 2, at a radius of 33 mm around a new, narrower, beam pipe. The calorimeters cover $|\eta| < 4.9$, with the forward region $(3.2 < |\eta| < 4.9)$ being instrumented with a liquid-argon (LAr) calorimeter for both the electromagnetic and hadronic measurements. In the central region, a lead/LAr electromagnetic calorimeter covers $|\eta| < 3.2$, while the hadronic calorimeter uses two different detector technologies, with scintillator tiles $(|\eta| < 1.7)$ or liquid argon $(1.5 < |\eta| < 3.2)$ as the active medium. The MS consists of three layers of precision tracking chambers providing coverage over $|\eta| < 2.7$, while dedicated fast chambers allow triggering over $|\eta| < 2.4$. The ATLAS trigger system used for real-time event selection (developed from Ref. [27]) consists of a hardware-based first-level trigger and a software based high-level trigger.

---

[1] ATLAS uses a right-handed coordinate system with its origin at the nominal interaction point (IP) in the centre of the detector and the z-axis along the beam pipe. The x-axis points from the IP to the centre of the LHC ring, and the y-axis points upward. Cylindrical coordinates (r, ϕ) are used in the transverse plane, ϕ being the azimuthal angle around the z-axis. The pseudorapidity is defined in terms of the polar angle θ as $\eta = -\ln\tan(\theta/2)$ and the rapidity is defined as $y = 0.5\ln[(E + p_z)/(E - p_z)]$, where E is the energy and p_z the longitudinal momentum of the object of interest.

Table 1: Simulated signal and background event samples: the corresponding generator, parton shower, cross-section normalisation, PDF set and underlying-event tune are shown.

Physics process	Generator	Parton shower	Cross-section	PDF set	Tune
Signal	MG5_aMC@NLO 2.2.2	Pythia 8.186	NLO+NLL	NNPDF2.3 LO	ATLAS A14
$t\bar{t}$	powheg-box v2	Pythia 6.428	NNLO+NNLL	CT10 NLO	Perugia2012
Single-top					
t-channel	powheg-box v1	Pythia 6.428	NLO	CT10f4 NLO	Perugia2012
s-channel	powheg-box v2	Pythia 6.428	NLO	CT10 NLO	Perugia2012
Wt-channel	powheg-box v2	Pythia 6.428	NLO+NNLL	CT10 NLO	Perugia2012
$W(\to \ell\nu)$ + jets	Sherpa 2.2.0	Sherpa 2.2.0	NNLO	NNPDF3.0 NNLO	Sherpa default
$Z/\gamma^*(\to \ell\ell)$ + jets	Sherpa 2.2.0	Sherpa 2.2.0	NNLO	NNPDF3.0 NNLO	Sherpa default
WW, WZ and ZZ	Sherpa 2.1.1	Sherpa 2.1.1	NLO	CT10 NLO	Sherpa default
$t\bar{t} + W/Z/WW$	MG5_aMC@NLO 2.2.2	Pythia 8.186	NLO	NNPDF2.3 LO	ATLAS A14

3 Simulated event samples and data samples

As in previous similar ATLAS searches [19, 20], simplified signal models are used. Sparticles (gluinos or squarks) are assumed to be produced exclusively in pairs ($\tilde{g}\tilde{g}$ or $\tilde{q}\bar{\tilde{q}}$) with subsequent decays with 100% branching ratio via an intermediate chargino (in this search the lightest chargino $\tilde{\chi}_1^\pm$) to the LSP (the lightest neutralino $\tilde{\chi}_1^0$). Other supersymmetric particles not entering the decay chain are not considered in this simplified model. Only first- and second-generation squarks are considered, hence no bottom or top quarks are produced along the decay chain of the simplified model. The free parameters of the model are the masses of the gluino/squark ($m_{\tilde{g}/\tilde{q}}$), the chargino ($m_{\tilde{\chi}_1^\pm}$) and the neutralino ($m_{\tilde{\chi}_1^0}$). To probe a broad range of SUSY particle mass spectra two model parameterisations are considered. In the first type, $m_{\tilde{g}/\tilde{q}}$ and the mass ratio $x \equiv (m_{\tilde{\chi}_1^\pm} - m_{\tilde{\chi}_1^0})/(m_{\tilde{g}/\tilde{q}} - m_{\tilde{\chi}_1^0})$ are free parameters, while $m_{\tilde{\chi}_1^0}$ is fixed to 60 GeV. In the second type, $m_{\tilde{g}/\tilde{q}}$ and $m_{\tilde{\chi}_1^0}$ are free parameters, while $m_{\tilde{\chi}_1^\pm}$ is fixed by setting $x = 1/2$.

The simulated event samples for the signal and SM backgrounds are summarised in Table 1. Additional samples are used to assess systematic uncertainties, as explained in Section 7.

The signal samples are generated using MG5_aMC@NLO 2.2.2 [28] with up to two extra partons in the matrix element, interfaced to Pythia 8.186 [29] for parton showers and hadronisation. The CKKW-L matching scheme [30] is applied for the combination of the matrix element and the parton shower, with a scale parameter set to a quarter of the mass of the sparticle. The ATLAS A14 [31] set of tuned parameters (tune) is used for the underlying event, together with the NNPDF2.3 LO [32] parton distribution function (PDF) set. The EvtGen v1.2.0 program [33] is used to describe the properties of the bottom and charm hadron decays in the signal samples.

The signal cross-sections are calculated at next-to-leading order (NLO) in the strong coupling constant, adding the resummation of soft gluon emission at next-to-leading-logarithmic accuracy (NLL) [34–38]. The nominal cross-section and its uncertainty are taken from an envelope of cross-section predictions using different PDF sets and factorisation and renormalisation scales [39, 40].

For the generation of $t\bar{t}$ and single top quarks in the Wt and s-channels [41] the powheg-box v2 [42] generator with the CT10 [43] PDF sets in the matrix-element calculations is used. Electroweak t-channel single-top-quark events are generated using the powheg-box v1 generator. This generator uses the four-flavour scheme for the NLO matrix-element calculations together with the fixed four-flavour PDF set

CT10f4. For all top-quark processes, top-quark spin correlations are preserved (for the single-top t-channel, top quarks are decayed using MadSpin [44]). The parton shower, fragmentation, and the underlying event are simulated using PYTHIA 6.428 [45] with the CTEQ6L1 [46] PDF set and the corresponding PERUGIA2012 tune (P2012) [47]. The top-quark mass is set to 172.5 GeV. The EvtGen v1.2.0 program is also used to describe the properties of the bottom and charm hadron decays in the $t\bar{t}$ and the single-top-quark samples. The hdamp parameter, which controls the p_{T} of the first additional emission beyond the Born configuration, is set to the mass of the top-quark. The main effect of this is to regulate the high p_{T} emission against which the $t\bar{t}$ system recoils. The $t\bar{t}$ events are normalised to the NNLO+NNLL cross-sections [48]. The single top quark events are normalised to the NLO+NNLL cross-sections for the Wt-channel [49] and to the NLO cross-sections for the t and s-channels [50].

Events containing W or Z bosons with associated jets (W/Z+jets) [51] are simulated using the SHERPA 2.2.0 generator [52] with massive b/c-quarks. Matrix elements are calculated for up to two partons at NLO and four partons at leading order (LO). The matrix elements are calculated using the Comix [53] and Open-Loops [54] generators and merged with the SHERPA 2.2.0 parton shower [55] using the ME+PS@NLO prescription [56]. The samples have been produced with a simplified scale setting prescription in the multi-parton matrix elements, to improve the event generation speed. A theory-based re-weighting of the jet multiplicity distribution is applied at event level, derived from event generation with the strict scale prescription. The NNPDF3.0 NNLO PDF set is used in conjunction with a dedicated parton-shower tuning developed by the SHERPA authors. The W/Z+jets events are normalised to their NNLO cross-sections [57].

The diboson samples [58] are generated using the SHERPA 2.1.1 generator with the same PDF setup as the W/Z+jets samples described above. The fully leptonic diboson processes are simulated including final states with four charged leptons, three charged leptons and one neutrino, two charged leptons and two neutrinos, and one charged lepton and three neutrinos. The matrix elements contain all diagrams with four electroweak vertices. They are calculated for up to one parton (4ℓ, $2\ell+2\nu$, ZZ) or no additional partons ($3\ell+1\nu$, $1\ell+3\nu$, WW, WZ) at NLO and up to three partons at LO. Each of the diboson processes is normalised to the corresponding NLO cross-section [58].

For the $t\bar{t} + W/Z/WW$ processes [59], all events are simulated using MG5_AMC@NLO 2.2.2 at LO interfaced to the PYTHIA 8.186 parton shower model, with up to two ($t\bar{t} + W$), one ($t\bar{t} + Z$) or no ($t\bar{t} + WW$) extra partons included in the matrix element. The ATLAS underlying-event tune A14 is used together with the NNPDF2.3 LO PDF set. The events are normalised to their respective NLO cross-sections [60, 61].

The response of the detector to particles is modelled either with a full ATLAS detector simulation [62] using GEANT4 [63] or with a fast simulation [64]. The fast simulation is based on a parameterisation of the performance of the electromagnetic and hadronic calorimeters and on GEANT4 elsewhere. All background (signal) samples are prepared using the full (fast) detector simulation.

All simulated samples are generated with a varying number of minimum-bias interactions overlaid on the hard-scattering event to model the multiple proton–proton interactions in the same and the nearby bunch crossings. The minimum-bias interactions are simulated with the soft QCD processes of PYTHIA 8.186 using the A2 tune [65] and the MSTW2008LO PDF set [66]. Corrections are applied to the simulated samples to account for differences between data and simulation for trigger, identification and reconstruction efficiencies.

The proton–proton data analysed in this paper were collected by ATLAS in 2015 and 2016 (before August 2016) at a centre-of-mass energy of 13 TeV. After application of data-quality requirements related to

the beam and detector conditions, the total integrated luminosity amounts to 14.8 fb^{-1}. The preliminary uncertainty on the combined 2015+2016 integrated luminosity is ±3.0%. It is derived, following a methodology similar to that detailed in Refs. [67] from a preliminary calibration of the luminosity scale using x-y beam-separation scans performed in August 2015 and May 2016.

The data are collected using a trigger that selects events based on the amount of E_T^{miss} calculated in the detector. The corresponding online reconstructed E_T^{miss} trigger thresholds were 70 GeV in the 2015 dataset and 100 GeV in the 2016 dataset. Both triggers are close to fully efficient after the requirement on the offline reconstructed E_T^{miss} to be larger than 200 GeV.

4 Object reconstruction and identification

The reconstructed primary vertex of an event is required to be consistent with the interaction region and to have at least two associated tracks with $p_T > 400$ MeV. When more than one such vertex is found, the vertex with the largest $\sum p_T^2$ of the associated tracks is chosen.

In the analysis, a distinction is made between *preselected* reconstructed objects, which fulfill a set of basic criteria and are used in the E_T^{miss} computation, and *signal* objects that enter the final analysis selections and are subject to more stringent requirements.

Jets are reconstructed from topological clusters in the calorimeters using the anti-k_t algorithm with a radius parameter $R = 0.4$ [68, 69]. Prior to jet reconstruction, clusters are calibrated to the electromagnetic scale [70]. Additional correction factors derived from simulation and data are applied to the measured jet energy to calibrate it to the particle level [69]. To mitigate the contributions from multiple interactions per proton bunch crossing (pile-up), the median energy density of all the jets in the event, multiplied by the jet area, is subtracted from the reconstructed jet energy [71, 72]. Preselected jets are required to have $p_T > 20$ GeV and $|\eta| < 4.5$.

To remove residual contamination of pile-up jets, a likelihood discriminant, the *jet-vertex tagger* (JVT), is constructed from track-based variables that are sensitive to the vertex of origin of the jet [73]. Jets with $p_T < 60$ GeV, $|\eta| < 2.4$, and JVT score less than 0.59 are rejected.

Signal jets are required to have $p_T > 30$ GeV and $|\eta| < 2.8$. Signal jets within $|\eta| < 2.5$ containing b-hadrons are identified using the *MV2c10* algorithm [74] and are hereafter referred to as b-tagged jets. The *MV2c10* algorithm uses as input the impact parameters of all associated tracks and any reconstructed secondary vertices. The requirement chosen in the analysis provides an inclusive b-tagging efficiency of 77% in simulated $t\bar{t}$ events, along with a rejection factor of 134 for gluon and light-quark jets and of 6.2 for charm jets [74, 75].

Electron candidates are reconstructed using ID tracks matched to energy clusters in the electromagnetic calorimeter. They are identified according to the likelihood-based *LooseAndBLayerLLH* criteria [76]. Preselected electrons must satisfy $p_T > 7$ GeV and $|\eta| < 2.47$.

Muon candidates are reconstructed by combining tracks formed in the ID and the MS subsystems. The *Medium* identification criteria are applied, which offer good efficiency and purity for the selected muons [77]. Preselected muons are required to have $p_T > 6$ GeV and $|\eta| < 2.5$.

A sequence of overlap-removal procedures are applied to preselected jets, electrons, and muons to resolve ambiguities in object identification. First, if an electron and a jet lie within $\Delta R < 0.2$, where $\Delta R =$

$\sqrt{(\Delta y)^2 + (\Delta \phi)^2}$, the jet is discarded and the electron is kept. This suppresses jets that are reconstructed from the electromagnetic cluster of an electron. Next, if an electron and a muon lie within $\Delta R < 0.01$, then the electron is discarded and the muon is kept. This removes electrons from muon bremsstrahlung followed by a photon conversion. If a muon and a jet lie within $\Delta R < 0.2$, then the jet is discarded and the muon is kept; unless the jet contains more than three tracks with $p_T > 500$ MeV and $p_T(\mu)/p_T(\text{jet}) < 0.7$, or the jet is b-tagged, in which case the muon is discarded and the jet is kept. Finally, if a muon and a jet lie within $\Delta R < \min(0.04 + (10 \text{ GeV})/p_T, 0.4)$, the muon is discarded and the jet is kept. The two last procedures suppress muons from heavy-hadron decays.

Signal muons and electrons must satisfy the *GradientLoose* [77] isolation requirements, which rely on the use of tracking-based and calorimeter-based variables and implement a set of η- and p_T-dependent criteria. The efficiency for prompt leptons with transverse momentum > 25 GeV (> 60 GeV) to satisfy the *GradientLoose* requirements is measured to be 95% (98%) in $Z \to \ell\ell$ events [77]. In addition, signal electrons must satisfy the likelihood-based *tight* identification criteria defined in Ref. [76].

To enforce compatibility with the primary vertex, the distance $|z_0 \cdot \sin(\theta)|$ is required to be less than 0.5 mm for signal lepton tracks, where z_0 is the longitudinal impact parameter with respect to the primary-vertex position. Moreover, in the transverse plane the distance of closest approach of the lepton track to the proton beam line, divided by the corresponding uncertainty, must be less than three for muons and less than five for electrons.

The missing transverse momentum E_T^{miss} is calculated as the magnitude of the negative vector sum p_T^{miss} of the transverse momenta of identified and calibrated muons, electrons, jets and photons, in addition to the *soft-track* term. The soft-track term is defined as the vectorial sum of the p_T of all reconstructed tracks associated with the primary vertex that are not associated with the identified objects explicitely entering the E_T^{miss} computation [78, 79].

Reconstruction, identification and isolation efficiencies in simulation, when applicable, are calibrated to data for all reconstructed objects.

5 Event selection

The triggered events are required to have a reconstructed primary vertex. Events with any preselected jet failing the quality criteria defined to suppress non-collisions backgrounds and detector noise [80] are rejected. Furthermore, exactly one signal electron or muon is required. Events with additional preselected leptons are rejected to suppress the dilepton $t\bar{t}$, single-top (Wt-channel) and diboson backgrounds.

Ten signal region (SR) selection criteria are designed to maximise the signal sensitivity. One low-p_T lepton ("soft-lepton") signal region is defined to target the gluino production scenarios with compressed mass spectra. Five gluino hard-lepton signal regions and four squark hard-lepton signal regions are defined, targeting different mass hierarchy scenarios for the gluino and squark signal models.

The observables used in the event selection are defined as below.

The transverse mass (m_T) of the lepton and the p_T^{miss} is defined as

$$m_T = \sqrt{2 p_T^\ell E_T^{\text{miss}} (1 - \cos[\Delta\phi(p_T^\ell, p_T^{\text{miss}})])}, \tag{1}$$

where $\Delta\phi(\boldsymbol{p}_\mathrm{T}^\ell, \boldsymbol{p}_\mathrm{T}^\mathrm{miss})$ is the azimuthal angle between the lepton and the missing transverse momentum. This observable is used for all the signal regions to reject W+jets and semileptonic $t\bar{t}$ events (containing a $W \rightarrow l\nu$ decay).

The inclusive effective mass ($m_\mathrm{eff}^\mathrm{inc}$) is the scalar sum of the p_T of the signal lepton and jets and the $E_\mathrm{T}^\mathrm{miss}$:

$$m_\mathrm{eff}^\mathrm{inc} = p_\mathrm{T}^\ell + \sum_{j=1}^{N_\mathrm{jet}} p_{\mathrm{T},j} + E_\mathrm{T}^\mathrm{miss}, \qquad (2)$$

where the index j runs over all the signal jets in the event with $p_\mathrm{T} > 30\,\mathrm{GeV}$. The inclusive effective mass provides good discrimination against SM backgrounds, especially for the signal scenarios where energetic jets are expected. This variable is used for five gluino hard-lepton signal regions and one squark hard-lepton signal region.

The ratio $E_\mathrm{T}^\mathrm{miss}/m_\mathrm{eff}^\mathrm{inc}$ is used in both the soft- and hard-lepton channels; it provides good discrimination power between signal and background with fake $E_\mathrm{T}^\mathrm{miss}$ due to instrumental effects. The signal usually exhibits larger values of $E_\mathrm{T}^\mathrm{miss}/m_\mathrm{eff}^\mathrm{inc}$ compared to the SM backgrounds due to the $E_\mathrm{T}^\mathrm{miss}$ from the neutralinos.

Additional suppression of background processes is based on the aplanarity variable, defined as $\mathcal{A} = \frac{3}{2}\lambda_3$, where λ_3 is the smallest eigenvalue of the normalised momentum tensor of the event [81]. Typical measured values lie in the range $0 \leqslant \mathcal{A} < 0.3$, with values near zero indicating relatively planar background-like events. Signal events tend to be more spherical than background events due to the many objects (jets, lepton, neutrino, neutralinos) emitted during the subsequent sparticles decay chains. Two varieties of this variable are used in the analysis: the 'jet aplanarity' is calculated using only the momenta of the jets in the event, while the 'lepton aplanarity' further includes the lepton momentum. The former is used in the gluino hard-lepton signal regions, and the latter in the squark hard-lepton signal regions. The difference between the two definitions of aplanarity is small for the gluino signal regions, which require a larger amount of hadronic energy than the squark signal regions. This choice was made to keep the definition of one of the gluino signal regions consistent with the previous analysis using the 2015 data [20], where a small excess of data events was observed.

The selection criteria for all signal regions are summarised in Table 2- 4. Each SR is labeled based on the envisaged sparticle production scenario (**GG** for gluino pair production and **SS** for squark pair production), the minimum number of signal jets (**2J**, **4J**, **5J**, and **6J**), and the characteristics of the targeted supersymmetric mass spectrum. The detailed descriptions on the motivation and selection criteria for each SR are discussed below.

- The selection criteria for the gluino soft-lepton signal region are summarised in Table 2. The **GG 2J** region provides sensitivity to scenarios characterised by a relatively heavy neutralino and small mass differences between $m_{\tilde{g}}$, $m_{\tilde{\chi}_1^\pm}$, and $m_{\tilde{\chi}_1^0}$, where most of the decay products tend to have small p_T. Sensitivity to the signal is enhanced by targeting events with initial-state radiation (ISR) jets with large p_T recoiling against the produced gluino pair. In such an event, the final-state neutralinos are boosted against the ISR jets, and give rise to large $E_\mathrm{T}^\mathrm{miss}$ that can be used to separate the signal from the SM backgrounds.

- The selection criteria for the gluino hard-lepton signal regions are summarised in Table 3. Of the five SRs targeting gluino pair production models, the **GG 6J bulk** and **GG 6J high-mass** SRs are optimised for models with $x = 1/2$, i.e., $m_{\tilde{\chi}_1^\pm} = (m_{\tilde{g}} + m_{\tilde{\chi}_1^0})/2$. Events with one high-$p_\mathrm{T}$ lepton and

Table 2: Overview of the selection criteria for the gluino soft-lepton signal region.

	GG 2J
N_{lep} (preselected)	= 1
p_{T}^{ℓ} (GeV)	[7(6), 35] for electron (muon)
N_{jet}	≥ 2
$p_{\text{T}}^{\text{jet1}}$ (GeV)	> 200
$p_{\text{T}}^{\text{jet2}}$ (GeV)	> 30
m_{T} (GeV)	> 100
$E_{\text{T}}^{\text{miss}}$ (GeV)	> 460
$E_{\text{T}}^{\text{miss}}/m_{\text{eff}}^{\text{inc}}$	> 0.35

six jets are selected and requirements on m_{T}, $E_{\text{T}}^{\text{miss}}$, $m_{\text{eff}}^{\text{inc}}$, and jet aplanarity are placed to reduce the SM background from $t\bar{t}$ and W + jets production. While SR **GG 6J bulk** targets the region of intermediate gluino and neutralino masses, SR **GG 6J high-mass** improves the sensitivity for scenarios with large $m_{\tilde{g}}$ and small $m_{\tilde{\chi}_1^0}$ using a more stringent requirement on $m_{\text{eff}}^{\text{inc}}$. The **GG 4J low-x**, **GG 4J low-x b-veto** and **GG 4J high-x** regions target models where $m_{\tilde{\chi}_1^0}$ is fixed to 60 GeV. The **GG 4J low-x** and **GG 4J low-x b-veto** SRs are optimised for scenarios with $x \approx 0$, i.e., $m_{\tilde{\chi}_1^\pm}$ is close to $m_{\tilde{\chi}_1^0}$. The large $m_{\tilde{g}}$–$m_{\tilde{\chi}_1^\pm}$ mass splitting produces four high-p_{T} jets, but m_{T} tends to be small. Thus a low p_{T} cut is placed on the lepton and these SRs cover both soft and hard lepton events. The background is further suppressed by tight requirements on $m_{\text{eff}}^{\text{inc}}$ and on the aplanarity. The **GG 4J low-x b-veto** SR rejects events containing b-jets to further reduce the $t\bar{t}$ background. This selection requirement improves the sensitivity in the phase-space of the targeted signal model and is applied to obtain the model-dependent limits. The **GG 4J low-x** SR is b-agnostic and is used to place model-independent limits on the visible cross section. The **GG 4J high-x** SR is optimised for scenarios with of $x \approx 1$, i.e., $m_{\tilde{\chi}_1^\pm}$ is close to $m_{\tilde{g}}$. The W boson produced in the chargino decay is significantly boosted, leading to a high-p_{T} lepton. The main characteristics of signal events in the phase-space of this model are large m_{T} values and relatively soft jets emitted from the gluino decay.

- The selection criteria for the squark hard-lepton signal regions are summarised in Table 4. Of the four SRs targeting squark pair production models, the first two SRs are designed to target models with $m_{\tilde{g}}$ and $m_{\tilde{\chi}_1^0}$ chosen freely, and with $m_{\tilde{\chi}_1^\pm}$ to satisfy $x = 1/2$. The **SS 4J x=1/2** SR is designed to target scenarios with large $m_{\tilde{q}}$ and small $m_{\tilde{\chi}_1^0}$. The **SS 5J x=1/2** SR is designed to provide sensitivity to the scenarios where the separation between $m_{\tilde{q}}$ and $m_{\tilde{\chi}_1^0}$ is small. Thus, a tight requirement on $m_{\text{eff}}^{\text{inc}}$ is applied to the **SS 4J x=1/2** SR while no $m_{\text{eff}}^{\text{inc}}$ requirement is applied to the **SS 5J x=1/2** SR. The last two SRs are designed to target models where $m_{\tilde{\chi}_1^0}$ is fixed to 60 GeV while $m_{\tilde{q}}$ and the mass-ratio parameter x vary. The **SS 4J low-x** region is designed for regions of the parameter space where the W boson tends to be virtual while the jets from the squark decays tend to have high p_{T} due to the large squark–chargino mass difference. The main characteristics of signal events in the phase-space of this model are a soft m_{T} spectrum and a harder jet p_{T} spectrum. In the **SS 5J high-x** region, the W boson produced in the chargino decay is significantly boosted, leading to high-p_{T} leptons. Therefore, the m_{T} requirement is tight and relatively soft jets are expected from the squark decays. For all the squark hard-lepton signal regions, events containing b-jets are rejected to further reduce $t\bar{t}$ background.

Table 3: Overview of the selection criteria for the gluino hard-lepton signal regions.

	GG 6J bulk	GG 6J high-mass	GG 4J low-x	GG 4J low-x b-veto	GG 4J high-x
N_{lep} (preselected)			= 1		
p_T^ℓ (GeV)	> 35	> 35	> 7(6) for electron (muon)	> 7(6) for electron (muon)	> 35
N_{jet}	≥ 6	≥ 6	≥ 4	≥ 4	≥ 4
p_T^{jet1} (GeV)	> 125	> 125	> 100	> 100	> 400
$p_T^{\text{jet2,3}}$ (GeV)	> 30	> 30	> 100	> 100	> 30
p_T^{jet4} (GeV)	> 30	> 30	> 100	> 100	[30, 100]
$p_T^{\text{jet5,6}}$ (GeV)	> 30	> 30	-	-	-
$N_{\text{b−jet}}$	-	-	-	= 0	-
m_T (GeV)	> 225	> 225	> 125	> 125	> 475
E_T^{miss} (GeV)	> 250	> 250	> 250	> 250	> 250
$m_{\text{eff}}^{\text{inc}}$ (GeV)	> 1000	> 2000	> 2000	> 2000	> 1600
$E_T^{\text{miss}}/m_{\text{eff}}^{\text{inc}}$	> 0.2	> 0.1	-	-	> 0.3
Jet aplanarity	> 0.04	> 0.04	> 0.06	> 0.03	-

Table 4: Overview of the selection criteria for the squark hard-lepton signal regions.

	SS 4J x=1/2	SS 5J x=1/2	SS 4J low-x	SS 5J high-x
N_{lep} (preselected)		= 1		
p_T^ℓ (GeV)		> 35		
N_{jet}	≥ 4	≥ 5	≥ 4	≥ 5
$p_T^{\text{jet1,2}}$ (GeV)	> 50	> 50	> 250	> 30
$p_T^{\text{jet3,4}}$ (GeV)	> 50	> 50	> 30	> 30
p_T^{jet5} (GeV)	-	> 50	-	> 30
$N_{\text{b−jet}}$		= 0		
m_T (GeV)	> 175	> 175	[150, 400]	> 400
E_T^{miss} (GeV)	> 300	> 300	> 250	> 400
$m_{\text{eff}}^{\text{inc}}$ (GeV)	> 1200	-	-	-
$E_T^{\text{miss}}/m_{\text{eff}}^{\text{inc}}$	-	> 0.2	-	-
Lepton aplanarity	> 0.08	-	> 0.03	> 0.03

6 Background estimation

The dominant Standard Model background processes in the signal regions targeting gluino production are $t\bar{t}$ and W+jets. The signal regions constructed for squark production also exhibit a significant contribution from diboson processes. The differential distributions arising from these major background processes as predicted from simulation are simultaneously normalised to the number of data events observed in dedicated control regions (CR), through the fitting procedure described in Section 8. The simulation is then used to extrapolate the measured background rates to the corresponding signal region.

The control regions are designed to have high purity in the background process of interest, a small contamination from the signal model and enough events to result in a small statistical uncertainty on the background prediction. Moreover, they are designed to have kinematic properties resembling as closely as possible those of the signal regions, in order to provide good estimates of the kinematics of background processes there. This procedure limits the impact of potentially large systematic uncertainties in the expected yields.

Additional sources of background events are single-top events (s-channel, t-channel and associated production with a W boson), Z+jets, and $t\bar{t}$ production in association with a W or a Z boson. Their contributions are estimated entirely using simulated event samples normalised to the most accurate theoretical cross-sections available. The same procedure is applied to diboson processes (WW, WZ, ZZ, $W\gamma$, $Z\gamma$) in all signal regions targeting gluino production.

The contribution from multi-jet processes with a misidentified lepton is found to be negligible once lepton isolation criteria and a stringent E_T^{miss} requirement are imposed. A data-driven matrix method, following the implementation described in Ref. [19], confirms that this background is consistent with zero. This is mainly a result of the improved lepton reconstruction and identification and the higher threshold on E_T^{miss} with respect to the previous searches performed in this final state [19]. As this background is found to be negligible it is ignored in all aspects of the analysis.

Tables 5-13 list the criteria that define the control regions corresponding to signal regions. For all signal regions dedicated $t\bar{t}$ and W+jets control regions are defined which are denoted with the acronyms TR and WR, respectively. The TR and WR are distinguished by requiring at least one or exactly zero b-tagged signal jet. The cross-contamination of $t\bar{t}$ and W+jets processes between these two types of control regions is accounted for in the fit. For the signal regions targeting squark production dedicated control regions for diboson processes are constructed which are denoted with the acronym DR in tables 10-13.

To gain confidence in the extrapolation from control to signal regions using simulated event samples, dedicated validation regions are defined for each set of control and signal regions. The selection criteria defining these validation regions are also defined in tables 5-13. The validation regions are designed to be kinematically close to the signal regions, with only a small contamination from the signal in the models considered in this search. The validation regions are not used to constrain parameters in the fit, but provide a statistically independent cross-check of the extrapolation.

Table 5: Overview of the control and validation region selection criteria corresponding to the signal region **GG 2J**. The $t\bar{t}$ and W+jets control regions are denoted with the acronyms TR and WR, respectively.

GG 2J	WR / TR	VR E_T^{miss}	VR m_T
N_{lep} (preselected)		= 1	
p_T^{ℓ} (GeV)		[7(6), 35] for electron (muon)	
N_{jet}		≥ 2	
p_T^{jet1} (GeV)		> 200	
p_T^{jet2} (GeV)		> 30	
N_{b-jet}	= 0 / $\geq$ 1	–	–
m_T (GeV)	$\in [40 - 80]$	$\in [40, 100]$	> 80
E_T^{miss} (GeV)	$\in [250 - 460]$	> 460	$\in [250, 460]$
E_T^{miss}/m_{eff}^{inc}	> 0.35	> 0.35	> 0.35

Table 6: Overview of the control and validation region selection criteria corresponding to the signal region **GG 4J low-x**. The $t\bar{t}$ and W+jets control regions are denoted with the acronyms TR and WR, respectively.

GG 4J low-x	WR / TR	VR m_{T}	VR Aplanarity
N_{lep} (preselected)		= 1	
p_{T}^{ℓ} (GeV)		> 7(6) for electron (muon)	
N_{jet}		≥ 4	
$p_{\mathrm{T}}^{\mathrm{jet1}}$ (GeV)		> 100	
$p_{\mathrm{T}}^{\mathrm{jet2,3}}$ (GeV)		> 100	
$p_{\mathrm{T}}^{\mathrm{jet4}}$ (GeV)		> 100	
$N_{\mathrm{b-jet}}$	= 0 / ≥ 1	−	−
m_{T} (GeV)	> 100	> 100	< 100
$E_{\mathrm{T}}^{\mathrm{miss}}$ (GeV)	> 250	> 250	> 250
$m_{\mathrm{eff}}^{\mathrm{inc}}$ (GeV)	> 2000	> 2000	> 2000
$E_{\mathrm{T}}^{\mathrm{miss}}/m_{\mathrm{eff}}^{\mathrm{inc}}$	−	< 0.35	−
Jet aplanarity	< 0.03	< 0.03	> 0.03

Table 7: Overview of the control and validation region selection criteria corresponding to the signal region **GG 4J high-x**. The $t\bar{t}$ and W+jets control regions are denoted with the acronyms TR and WR, respectively.

GG 4J high-x	WR / TR	VR m_{T}	VR $E_{\mathrm{T}}^{\mathrm{miss}}/m_{\mathrm{eff}}^{\mathrm{inc}}$
N_{lep} (preselected)		= 1	
p_{T}^{ℓ} (GeV)		> 35	
N_{jet}		≥ 4	
$p_{\mathrm{T}}^{\mathrm{jet1}}$ (GeV)		> 400	
$p_{\mathrm{T}}^{\mathrm{jet2,3}}$ (GeV)		> 30	
$p_{\mathrm{T}}^{\mathrm{jet4}}$ (GeV)		[30, 100]	
$p_{\mathrm{T}}^{\mathrm{jet6}}$ (GeV)	−	< 30	−
$N_{\mathrm{b-jet}}$	= 0 / ≥ 1	−	−
m_{T} (GeV)	< 100	> 100	< 100
$E_{\mathrm{T}}^{\mathrm{miss}}$ (GeV)	> 250	> 250	> 250
$m_{\mathrm{eff}}^{\mathrm{inc}}$ (GeV)	> 1600	> 1600	> 1600
$E_{\mathrm{T}}^{\mathrm{miss}}/m_{\mathrm{eff}}^{\mathrm{inc}}$	< 0.3	< 0.3	> 0.3

Table 8: Overview of the control and validation region selection criteria corresponding to the signal region **GG 6J bulk**. The $t\bar{t}$ and W+jets control regions are denoted with the acronyms TR and WR, respectively.

GG 6J bulk	WR / TR	VR m_{T}	VR Aplanarity
N_{lep} (preselected)		= 1	
p_{T}^{ℓ} (GeV)		> 35	
N_{jet}		≥ 6	
$p_{\mathrm{T}}^{\mathrm{jet1}}$ (GeV)		> 125	
$p_{\mathrm{T}}^{\mathrm{jet2,3}}$ (GeV)		> 30	
$p_{\mathrm{T}}^{\mathrm{jet4}}$ (GeV)		> 30	
$p_{\mathrm{T}}^{\mathrm{jet5,6}}$ (GeV)		> 30	
$N_{\mathrm{b-jet}}$	= 0 / ≥ 1	–	–
m_{T} (GeV)	$\in [60, 125]$	$\in [125, 300]$	$\in [60, 125]$
$E_{\mathrm{T}}^{\mathrm{miss}}$ (GeV)	> 250	$\in [250, 400]$	> 250
$m_{\mathrm{eff}}^{\mathrm{inc}}$ (GeV)	> 1000	> 1000	> 1000
$E_{\mathrm{T}}^{\mathrm{miss}}/m_{\mathrm{eff}}^{\mathrm{inc}}$	> 0.2	> 0.2	> 0.2
Jet aplanarity	< 0.04	< 0.04	> 0.04

Table 9: Overview of the control and validation region selection criteria corresponding to the signal region **GG 6J high-mass**. The $t\bar{t}$ and W+jets control regions are denoted with the acronyms TR and WR, respectively.

GG 6J high-mass	WR / TR	VR m_{T}	VR Aplanarity
N_{lep} (preselected)		= 1	
p_{T}^{ℓ} (GeV)		> 35	
N_{jet}		≥ 6	
$p_{\mathrm{T}}^{\mathrm{jet1}}$ (GeV)		> 125	
$p_{\mathrm{T}}^{\mathrm{jet2,3}}$ (GeV)		> 30	
$p_{\mathrm{T}}^{\mathrm{jet4}}$ (GeV)		> 30	
$p_{\mathrm{T}}^{\mathrm{jet5,6}}$ (GeV)		> 30	
$N_{\mathrm{b-jet}}$	= 0 / ≥ 1	–	–
m_{T} (GeV)	$\in [60, 125]$	$\in [125, 350]$	$\in [60, 125]$
$E_{\mathrm{T}}^{\mathrm{miss}}$ (GeV)	> 200	> 250	> 250
$m_{\mathrm{eff}}^{\mathrm{inc}}$ (GeV)	> 1500	> 1500	> 1500
$E_{\mathrm{T}}^{\mathrm{miss}}/m_{\mathrm{eff}}^{\mathrm{inc}}$	> 0.1	> 0.1	> 0.1
Jet aplanarity	< 0.04	< 0.04	> 0.04

Table 10: Overview of the control and validation region selection criteria corresponding to the signal region **SS 4J x=1/2**. The $t\bar{t}$, W+jets, and diboson control regions are denoted with the acronyms TR, WR, and DR, respectively. The diboson validation region (denoted DVR) contains a same-sign (SS) lepton requirement for two-lepton events.

SS 4J x=1/2	WR / TR	DR	VR m_T	VR Aplanarity	DVR
N_{lep} (preselected)	= 1	≥ 2	= 1	= 1	= 2 SS or ≥ 3
p_T^{ℓ}(GeV)	> 35	> 7(6) for electron (muon)	> 35	> 35	> 7(6) for electron (muon)
N_{jet}	≥ 4	≥ 2	≥ 4	≥ 4	≥ 2
$p_T^{\text{jet1,2}}$ (GeV)	> 50	> 30	> 50	> 50	> 30
$p_T^{\text{jet3,4}}$ (GeV)	> 50	-	> 50	> 50	-
$N_{\text{b-jet}}$	= 0 / ≥ 1	= 0	= 0	= 0	= 0
m_T (GeV)	$\in [50, 100]$	$\in [50, 100]$	> 100	$\in [50, 150]$	> 100
E_T^{miss} (GeV)	> 300	> 250	> 200	> 300	> 250
$m_{\text{eff}}^{\text{inc}}$ (GeV)	> 1200	–	> 1200	> 1200	–
Lepton aplanarity	< 0.08	–	< 0.05	> 0.08	–

Table 11: Overview of the control and validation region selection criteria corresponding to the signal region **SS 5J x=1/2**. The $t\bar{t}$, W+jets, and diboson control regions are denoted with the acronyms TR, WR, and DR, respectively. The diboson validation region (denoted DVR) contains a same-sign (SS) lepton requirement for two-lepton events.

SS 5J x=1/2	WR / TR	DR	VR m_T	VR E_T^{miss}	DVR
N_{lep} (preselected)	= 1	≥ 2	= 1	= 1	= 2 SS or ≥ 3
p_T^{ℓ}(GeV)	> 35	> 7(6) for electron (muon)	> 35	> 35	> 7(6) for electron (muon)
N_{jet}	≥ 5	≥ 3	≥ 5	≥ 5	≥ 3
$p_T^{\text{jet1,2,3}}$ (GeV)	> 50	> 30	> 30	> 50	> 30
$p_T^{\text{jet4,5}}$ (GeV)	> 50	-	> 30	> 50	-
$N_{\text{b-jet}}$	= 0 / ≥ 1	= 0	= 0	= 0	= 0
m_T (GeV)	$\in [50, 100]$	$\in [50, 150]$	> 100	$\in [50, 100]$	> 150
E_T^{miss} (GeV)	$\in [200, 300]$	> 200	$\in [200, 300]$	> 300	> 200
$E_T^{\text{miss}}/m_{\text{eff}}^{\text{inc}}$	> 0.2	–	–	> 0.2	–

Table 12: Overview of the control and validation region selection criteria corresponding to the signal region **SS 4J low-x**. The $t\bar{t}$, W+jets, and diboson control regions are denoted with the acronyms TR, WR, and DR, respectively. The diboson validation region (denoted DVR) contains a same-sign (SS) lepton requirement for two-lepton events.

SS 4J low-x	WR / TR	DR	VR m_{T}	VR Aplanarity	DVR
N_{lep} (preselected)	= 1	≥ 2	= 1	= 1	= 2 SS or ≥ 3
p_{T}^{ℓ}(GeV)	> 35	> 7(6) for electron (muon)	> 35	> 35	> 7(6) for electron (muon)
N_{jet}	≥ 4	≥ 2	≥ 4	≥ 4	≥ 2
$p_{\mathrm{T}}^{\mathrm{jet1,2}}$ (GeV)	> 250	> 30	> 30	> 250, 200	> 30
$p_{\mathrm{T}}^{\mathrm{jet3,4}}$ (GeV)	> 30	-	> 30	> 30	-
$N_{\mathrm{b-jet}}$	= 0 / ≥ 1	= 0	= 0	= 0	= 0
m_{T} (GeV)	∈ [50, 100]	∈ [50, 100]	∈ [150, 400]	∈ [50, 100]	> 100
$E_{\mathrm{T}}^{\mathrm{miss}}$ (GeV)	> 250	> 250	> 200	> 250	> 250
Lepton aplanarity	< 0.03	–	< 0.03	> 0.03	–

Table 13: Overview of the control and validation region selection criteria corresponding to the signal region **SS 5J high-x**. The $t\bar{t}$, W+jets, and diboson control regions are denoted with the acronyms TR, WR, and DR, respectively. The diboson validation region (denoted DVR) contains a same-sign (SS) lepton requirement for two-lepton events.

SS 5J high-x	WR / TR	DR	VR m_{T}	VR Aplanarity	DVR
N_{lep} (preselected)	= 1	≥ 2	= 1	= 1	= 2 SS or ≥ 3
p_{T}^{ℓ}(GeV)	> 35	> 7(6) for electron (muon)	> 35	> 35	> 7(6) for electron (muon)
N_{jet}	≥ 5	≥ 3	≥ 5	≥ 5	≥ 3
$p_{\mathrm{T}}^{\mathrm{jet1,2,3}}$ (GeV)	> 30	> 30	> 30	> 30	> 30
$p_{\mathrm{T}}^{\mathrm{jet4,5}}$ (GeV)	> 30	-	> 30	> 30	-
$N_{\mathrm{b-jet}}$	= 0 / ≥ 1	= 0	= 0	= 0	= 0
m_{T} (GeV)	∈ [50, 100]	∈ [50, 150]	> 100	∈ [50, 150]	∈ [50, 150]
$E_{\mathrm{T}}^{\mathrm{miss}}$ (GeV)	> 400 / > 300	> 200	> 200	> 400	> 200
Lepton aplanarity	< 0.03	–	< 0.03	> 0.03	–

7 Systematic uncertainties

Two categories of systematic uncertainties have an impact on the results presented here: uncertainties arising from experimental effects, and uncertainties associated with theoretical predictions and modelling. Their effects are evaluated for all signal samples and background processes. Since the normalisation of the dominant background processes is extracted in dedicated control regions, the systematic uncertainties only affect the extrapolation to the signal regions in these cases. In all other cases, uncertainties on the inclusive cross-section for each specific process considered and on the acceptance of the analysis selection criteria are separately accounted for.

Among the dominant experimental systematic uncertainties are the jet energy scale (JES) and resolution (JER) and the muon momentum resolution. The jet uncertainties are derived as a function of p_T and η of the jet, as well as of the pile-up conditions and the jet flavour composition of the selected jet sample. They are determined using a combination of simulated samples and studies of data, such as measurements of the jet balance in dijet, Z+jet and γ+jet events [70]. The $J/\psi \to \ell^+\ell^-$, $W^\pm \to \ell^\pm\nu$ and $Z \to \ell^+\ell^-$ decays in data and simulation are exploited to estimate the uncertainties in lepton reconstruction, identification, momentum/energy scale and resolution, and isolation criteria [76, 77]. In particular, muon momentum resolution and scale calibrations are derived for simulation from a template fit that compares the invariant mass of $Z \to \mu\mu$ and $J/\psi \to \mu\mu$ candidates in data and simulation. The corresponding uncertainties are computed from variations of several fit parameters, following the procedure described in Ref. [82].

The simulation is reweighted to match the distribution of the average number of proton-proton interactions per bunch crossing observed in data (μ). In the signal regions characterised by a higher jet multiplicity, the uncertainty arising from this reweighting also becomes relevant: it is computed by varying up and down the reweighting factor to account for the uncertainty on μ itself.

The systematic uncertainties related to the modelling of E_T^{miss} in the simulation are estimated by propagating the uncertainties on the energy and momentum scale of each of the objects entering the calculation, as well as the uncertainties on the soft term resolution and scale.

Different uncertainties in the theoretical modelling of the SM production processes are considered, as described in the following.

For $t\bar{t}$, single-top and W/Z+jets samples, the uncertainties related to the choice of QCD renormalisation and factorisation scales are assessed by varying the corresponding generator parameters up and down by a factor of two around their nominal values. Uncertainties in the resummation scale and the matching scale between the matrix elements and parton shower are evaluated for the W+jets samples by varying up and down by a factor of two the corresponding parameters in Sherpa .

For $t\bar{t}$ and single-top production, specific samples with an increased and decreased amount of initial- and final-state radiation are compared to the nominal sample. The relative difference in the extrapolation factors ($t\bar{t}$) or expected rates (single-top) is assigned as an uncertainty. Moreover, the uncertainty associated with the parton shower modelling is assessed as the difference between the predictions from powheg with Pythia 6.428 and with Herwig++ 2.7.1 [83].

An uncertainty arising from the choice of parton level generator is estimated for $t\bar{t}$, diboson and W/Z+jets processes. For $t\bar{t}$, the predictions from powheg-box are compared with aMc@NLO 2.1.1 [84]. For dibosons, Sherpa is compared with powheg-box. For W/Z+jets, Sherpa is compared with Madgraph [85].

For $t\bar{t}$ and W+jets samples, the uncertainties on the transfer factors from CR to VR and SR associated to the choice of the PDF set, CT10 [43], are considered.

The uncertainty in the inclusive Z+jets cross-section is accounted for [86]. Similarly, uncertainties in the inclusive single-top cross-sections are assigned separately for the s-channel, t-channel and Wt-channel production [50]. Samples using diagram subtraction and diagram removal [87] schemes are compared for assessing the sensitivity to the treatment of interference effects between single-top and $t\bar{t}$ production at NLO.

An overall systematic uncertainty in the inclusive cross-section is assigned to the small contribution from WW, WZ, ZZ, $W\gamma$ and $Z\gamma$ processes in the gluino regions, where they are estimated entirely from simulation. The uncertainty accounts for missing higher-order corrections, for the uncertainty in the value of the strong coupling constant, and for the uncertainties on the PDF sets. The uncertainties associated with the resummation, factorisation and renormalisation scales are computed for gluino and squark regions by varying the corresponding SHERPA parameters.

For the very small contributions of $t\bar{t} + W/Z/WW$, an uncertainty of 30% is assigned.

Among the main systematic uncertainties on the total background predictions in the various signal regions are the ones associated with the finite size of the MC samples, which range from 4% in the **GG 2J** SR to 21% in the **GG 4J low-x** SR. Moreover, the uncertainties associated with the diboson background, range from 5% in the **GG 6J high-mass** SR to 24% in the **SS 4J x=1/2** SR. Further important uncertainties are the theoretical uncertainties associated with the single-top background, which amount to 3% in the **SS 5J high-x** SR and increase to as much as 25% in the **GG 4J low-x** SR, and the normalisation uncertainties on the $t\bar{t}$ (up to 16%) and W+jets (up to 16%) backgrounds.

The theoretical systematic uncertainty affecting the modelling of ISR can become sizeable in the simplified signal models used in this analysis, especially when the mass splittings between SUSY particles become small. Variations of a factor of two in the following MADGRAPH and PYTHIA parameters are used to estimate these uncertainties: the renormalisation and factorisation scales, the initial- and the final-state radiation scales, as well as the MADGRAPH jet matching scale. The overall uncertainties range from about 4% for signal models with large mass differences between the gluino or squark, the chargino, and the neutralino, to 15% for models with very compressed mass spectra.

8 Statistical analysis

The statistical interpretation of the results is performed using the profile likelihood method [88] implemented in the HistFitter framework [89].

Each SR is analysed in combination with its associated CRs and VRs, independently from other SRs. Three types of fits are performed for each SR to obtain the results presented in Section 9.

- A *background-only* fit uses the data event yields in the CRs to determine the background normalisation factors for $t\bar{t}$, W + jets, and diboson (in the case of squark SRs) production. The signal is assumed to be absent in this fit. The fit result predicts the SM event yield in the SR and the VRs using the transfer factors obtained from simulation.

- A *model-independent limit* fit combines the data event yield in the SR with the SM background estimate and its uncertainties obtained by the background-only fit to test the presence of any beyond-the-Standard-Model (BSM) physics that contributes to the SR. The BSM signal is assumed to contribute only to the SR and not to the CRs. Presence of a BSM signal can manifest itself in a small discovery p-value, which quantifies the statistical compatibility between the observed data event yield and the background estimate in the SR. An upper limit is also set on the visible cross section, a product of the production cross section and the acceptance and selection efficiency, of any BSM signal.

- A *model-dependent limit* fit uses the data event yields in the SR and the CRs to produce a limit on a specific SUSY model. The fit includes the expected SUSY signal contributions to the SR and to the CRs, scaled by a floating signal normalisation factor. The background normalisation factors are also determined simultaneously in the fit. A SUSY model with a specific set of sparticle masses is rejected if the upper limit of the signal normalisation factor obtained in this fit is smaller than unity.

The likelihood function is a product of Poisson probability density functions, one for each region (SR and CRs) contributing to the fit. The inputs to the likelihood function are the observed numbers of data events and the expected numbers of signal and SM background events in each region. One fit parameter is introduced as the normalisation factor for each of the signal, $t\bar{t}$, W + jets, and diboson (in squark SRs) expectations. Contributions from other, small, sources of SM background are taken directly from simulation. The systematic uncertainties described in Section 7 are incorporated into the fit through nuisance parameters constrained by Gaussian functions. The nuisance parameters are common across the SR and the CRs to account for the correlation of the systematic uncertainties. The uncertainties due to the finite statistics of the simulated samples are considered through nuisance parameters constrained by Poisson functions.

9 Results

The background yields in the validation and signal regions are calculated using the background-only fit described in Section 8. The comparisons between data and fitted background estimates are shown in Figure 2 for the VRs and Figure 3 for the SRs. The background estimates agree well with the data in all regions.

The normalisation of the $t\bar{t}$, W+jets and diboson backgrounds is adjusted in the background-only fits to match the data in the control regions. The fitted normalisation factors for $t\bar{t}$ are between $0.58^{+0.18}_{-0.16}$ and $1.08^{+0.24}_{-0.21}$. The W+jets background is adjusted by factors between $0.42^{+0.22}_{-0.17}$ and $1.03^{+0.03}_{-0.03}$, while the diboson background is scaled by factors between $1.09^{+0.54}_{-0.59}$ and $1.41^{+0.43}_{-0.45}$.

The background estimates in the signal regions are further detailed in Tables 14-15. In the **GG 6J bulk** signal region an excess of 2.1σ was observed in the 2015 data alone [20]. In the combined data 2015-2016 the data are compatible with the prediction at 1.2σ. No excess is present in events with an electron, while an excess of 1.8σ is seen in the muon channel.

Figures 4-5 show the distributions of m_{T}, $E_{\mathrm{T}}^{\mathrm{miss}}$ and of the lepton or jet aplanarity in the signal regions before applying the cut on the variable plotted.

Using the results of the background-only fit, model-independent observed and expected upper limits are derived at 95% confidence level (CL) on the number of events signifying new phenomena beyond the

Table 14: Background fit results for the gluino regions, for an integrated luminosity of 14.8 fb^{-1}. Uncertainties in the fitted background estimates combine statistical (in the simulated event yields) and systematic uncertainties. The uncertainties in this table are symmetrised for propagation purposes but truncated at zero to remain within the physical boundaries.

Region (GG)	2J	6J bulk	6J high-mass	4J low-x	4J low-x b-veto	4J high-x
Observed events	47	32	3	4	2	2
Fitted background events	46 ± 7	24 ± 5	3.8 ± 1.2	6.0 ± 1.6	3.3 ± 1.2	3.4 ± 0.9
Fitted $t\bar{t}$ events	12.4 ± 3.5	17 ± 5	2.0 ± 0.9	3.4 ± 1.6	0.8 ± 0.4	0.7 ± 0.4
Fitted W+jets events	16.7 ± 3.2	1.2 ± 0.5	0.6 ± 0.4	0.7 ± 0.4	1.2 ± 0.7	1.4 ± 0.4
Fitted Z+jets events	2.9 ± 1.7	$0.04^{+0.07}_{-0.04}$	0.11 ± 0.09	0.11 ± 0.08	0.030 ± 0.030	0.040 ± 0.030
Fitted single top events	3.4 ± 2.8	2.0 ± 1.6	0.7 ± 0.6	1.2 ± 1.0	1.0 ± 0.9	0.6 ± 0.5
Fitted diboson events	9 ± 5	1.8 ± 1.5	$0.20^{+0.33}_{-0.20}$	$0.21^{+0.32}_{-0.21}$	$0.31^{+0.33}_{-0.31}$	0.6 ± 0.6
Fitted $t\bar{t}$+V events	1.27 ± 0.12	1.72 ± 0.32	0.18 ± 0.06	0.27 ± 0.05	0.04 ± 0.010	0.18 ± 0.04

Table 15: Background fit results for the squark regions, for an integrated luminosity of 14.8 fb^{-1}. Uncertainties in the fitted background estimates combine statistical (in the simulated event yields) and systematic uncertainties. The uncertainties in this table are symmetrised for propagation purposes but truncated at zero to remain within the physical boundaries.

Region (SS)	4J x=1/2	5J x=1/2	4J low-x	5J high-x
Observed events	6	8	8	7
Fitted background events	5.4 ± 1.7	13.2 ± 2.5	11.1 ± 2.7	4.6 ± 1.4
Fitted $t\bar{t}$ events	1.0 ± 0.5	4.2 ± 1.5	1.8 ± 1.0	0.51 ± 0.20
Fitted W+jets events	2.2 ± 0.6	3.6 ± 0.9	4.0 ± 1.1	2.4 ± 0.8
Fitted Z+jets events	0.08 ± 0.06	0.29 ± 0.19	0.16 ± 0.09	0.11 ± 0.08
Fitted single top events	0.27 ± 0.24	0.6 ± 0.5	1.4 ± 1.2	0.18 ± 0.17
Fitted diboson events	1.8 ± 1.5	4.3 ± 2.5	3.7 ± 2.1	0.6 ± 0.6
Fitted $t\bar{t}$+V events	0.059 ± 0.022	0.34 ± 0.08	0.13 ± 0.04	0.104 ± 0.031

SM (S^{95}_{obs} and S^{95}_{exp}, respectively), as discussed in Section 8. All limits are calculated using the CL_s prescription [90]. Table 16 presents the upper limits together with the upper limits on the visible beyond the SM cross-section (σ_{vis}, defined as the product of acceptance, selection efficiency and production cross-section). The latter is calculated by dividing the observed upper limit on the number of beyond-SM events by the integrated luminosity of 14.8 fb^{-1}. The table also gives the background-only confidence level CL_b. Further, the discovery p-values are given, presenting the probability for the background-only assumption to produce event yields greater or equal to the observed data. The CL_b and p-values use different definitions of test statistics in their calculation, the former with the signal-strength parameter set to one and the latter to zero.

Using the model-dependent limit fit described in Section 8, limits on the specific models discussed in Section 3 are calculated. Figure 6 shows the combined 95% CL exclusion limits, where the signal region with the best expected sensitivity is used for each model point. Figure 7 details the contributions of the

Table 16: The columns show from left to right: the name of the respective signal region; the observed 95% confidence level (CL) upper limits on the visible cross-section ($\langle\epsilon\sigma\rangle_{\mathrm{obs}}^{95}$) and on the number of signal events (S_{obs}^{95}); the 95% CL upper limit on the number of signal events (S_{exp}^{95}), given the expected number (and $\pm 1\sigma$ variations on the expectation) of background events; the two-sided CL_b value, i.e. the confidence level observed for the background-only hypothesis and the one-sided discovery p-value ($p(s = 0)$). The discovery p-values are capped to 0.5 in the case of observing less events than the fitted background estimates.

Region	$\langle\epsilon\sigma\rangle_{\mathrm{obs}}^{95}$[fb]	S_{obs}^{95}	S_{exp}^{95}	CL_B	$p(s = 0)$
GG 2J	1.44	21.3	$20.2^{+6.8}_{-5.1}$	0.56	0.41
GG 6J bulk	1.49	22.1	$14.7^{+6.3}_{-4.2}$	0.89	0.11
GG 6J high-mass	0.35	5.1	$5.5^{+2.2}_{-1.4}$	0.40	0.90
GG 4J high-x	0.28	4.2	$5.2^{+2.2}_{-1.2}$	0.26	0.77
GG 4J low-x	0.37	5.5	$6.6^{+2.7}_{-1.7}$	0.28	0.83
SS 4J x=1/2	0.51	7.5	$6.9^{+2.8}_{-1.7}$	0.62	0.40
SS 5J x=1/2	0.43	6.3	$9.1^{+3.4}_{-2.4}$	0.13	0.88
SS 4J low-x	0.59	8.8	$6.6^{+2.5}_{-1.6}$	0.83	0.18
SS 5J high-x	0.49	7.2	$8.8^{+3.5}_{-2.1}$	0.26	0.91

various signal regions to the combined limits.

Depending on the model, gluino masses up to ∼ 1.8 TeV can be excluded for small LSP masses or chargino masses of ∼ 900 GeV. In the case of squark pair-production, the limits reach up to ∼ 1.1 TeV in the model parametrisation with fixed LSP mass at 60 GeV for chargino masses of ∼ 480 GeV or ∼ 650 GeV and also in the model parametrisation with fixed x for small LSP masses.
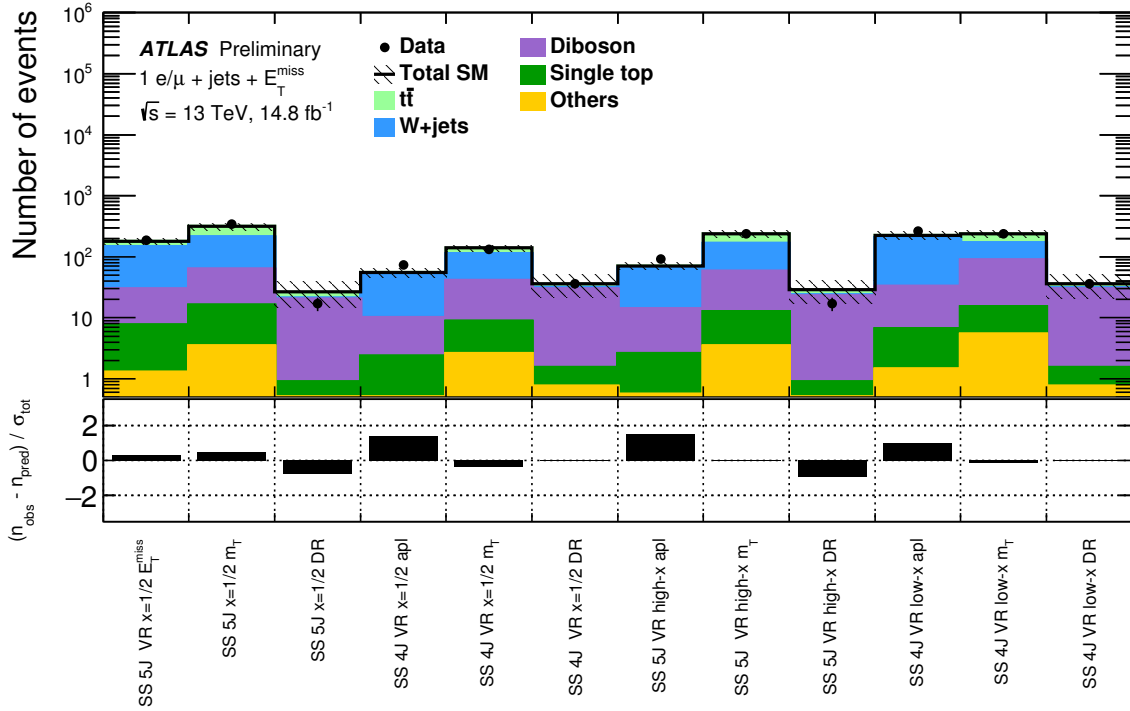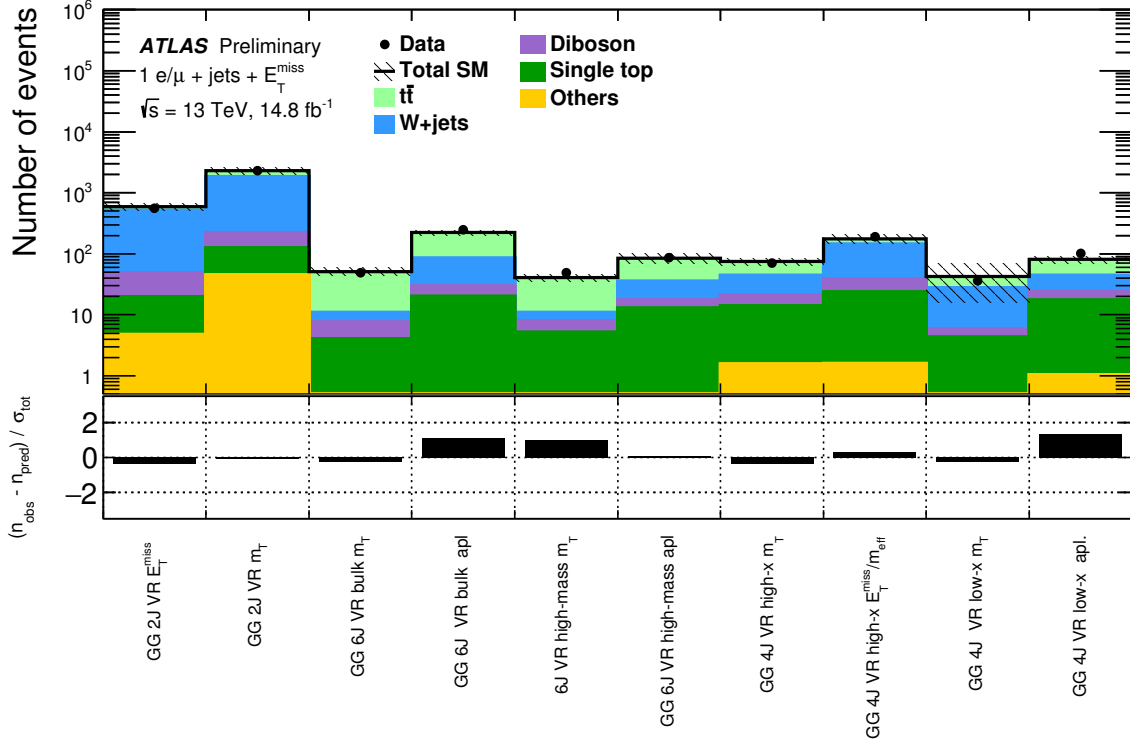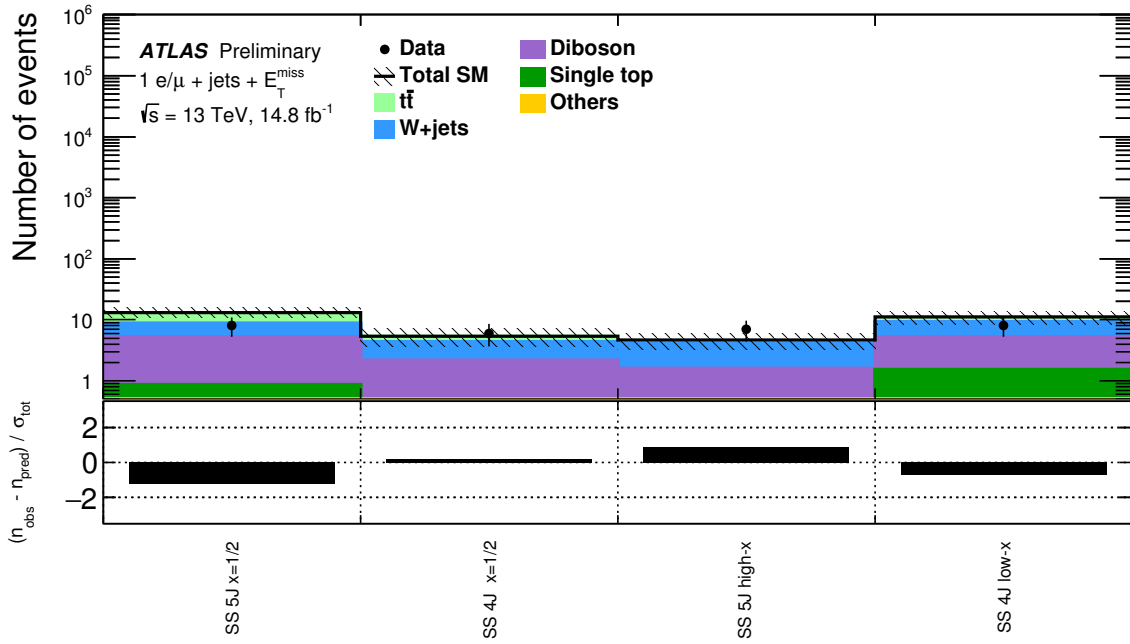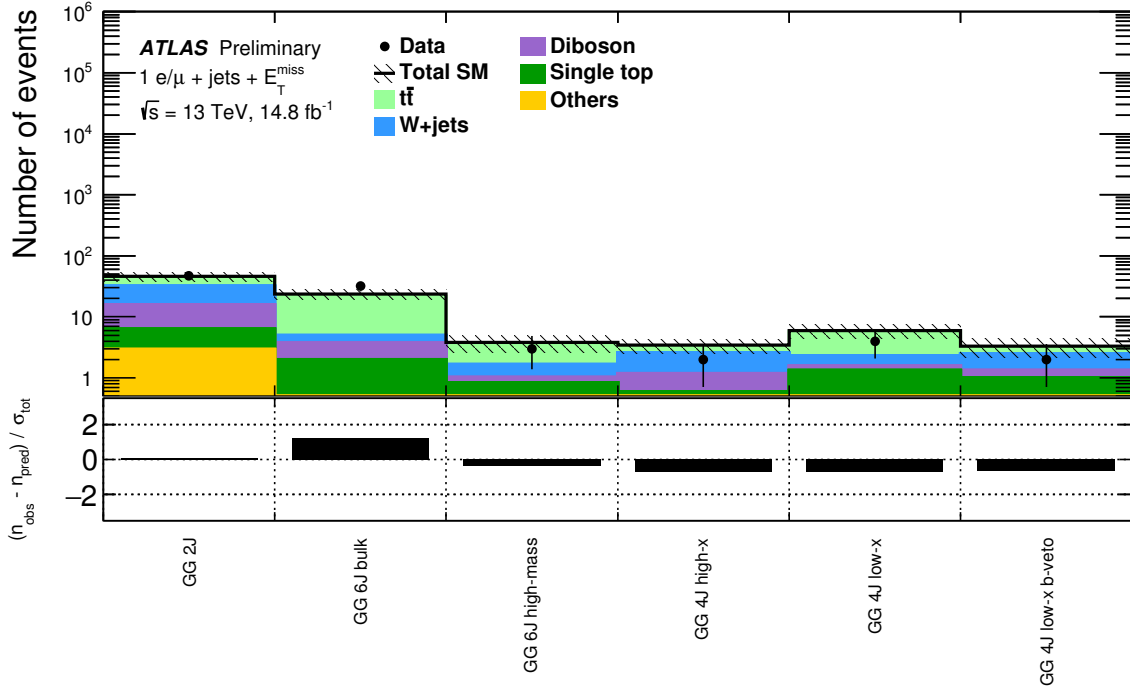
Figure 2: Expected background yields as obtained in the background-only fits in gluino (top plot) and squark (bottom plot) validation regions together with observed data are given in the top parts of the plots. Uncertainties in the fitted background estimates include both statistical (in the simulated event yields) and systematic uncertainties. The bottom parts of the plots show the differences between observed (n_{obs}) and predicted (n_{pred}) event yields, divided by the total uncertainty in the prediction (σ_{tot}).

Figure 3: Expected background yields as obtained in the background-only fits in gluino (top plot) and squark (bottom plot) signal regions together with observed data are given in the top parts of the plots. Uncertainties in the fitted background estimates include both statistical (in the simulated event yields) and systematic uncertainties. The bottom parts of the plots show the differences between observed (n_{obs}) and predicted (n_{pred}) event yields, divided by the total uncertainty in the prediction (σ_{tot}).
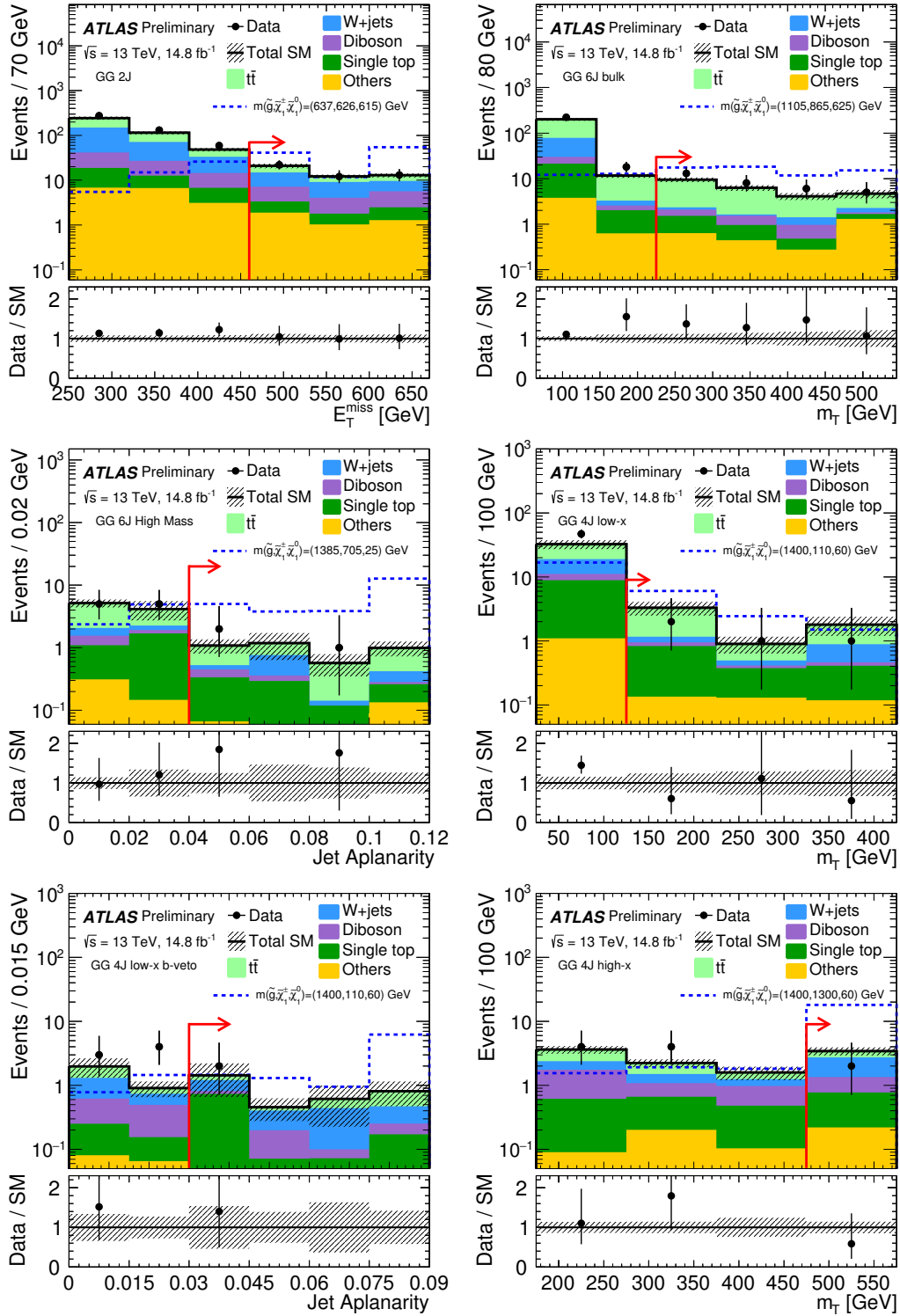
Figure 4: Distributions of E_T^{miss} for the **GG 2J** (top left) signal region, m_T for the **GG 6J bulk** (top right), **GG 4J low-x** (middle right) and **GG 4J high-x** (bottom right) signal regions and of the jet aplanarity for the **GG 6J high-mass** (middle left) and **GG 4J low-x b-veto** (bottom left) signal regions. The requirement on the variable plotted is removed from the definitions of the signal regions, where the arrow indicates the position of the cut in the signal region. The lower panels of the plots show the ratio of the observed data to the total background prediction as derived in the background-only fit. The uncertainty bands plotted include all statistical and systematic uncertainties as discussed in Section 7. The component 'Others' is the sum of Z+jets and $t\bar{t}$+V. The last bin includes the overflow.
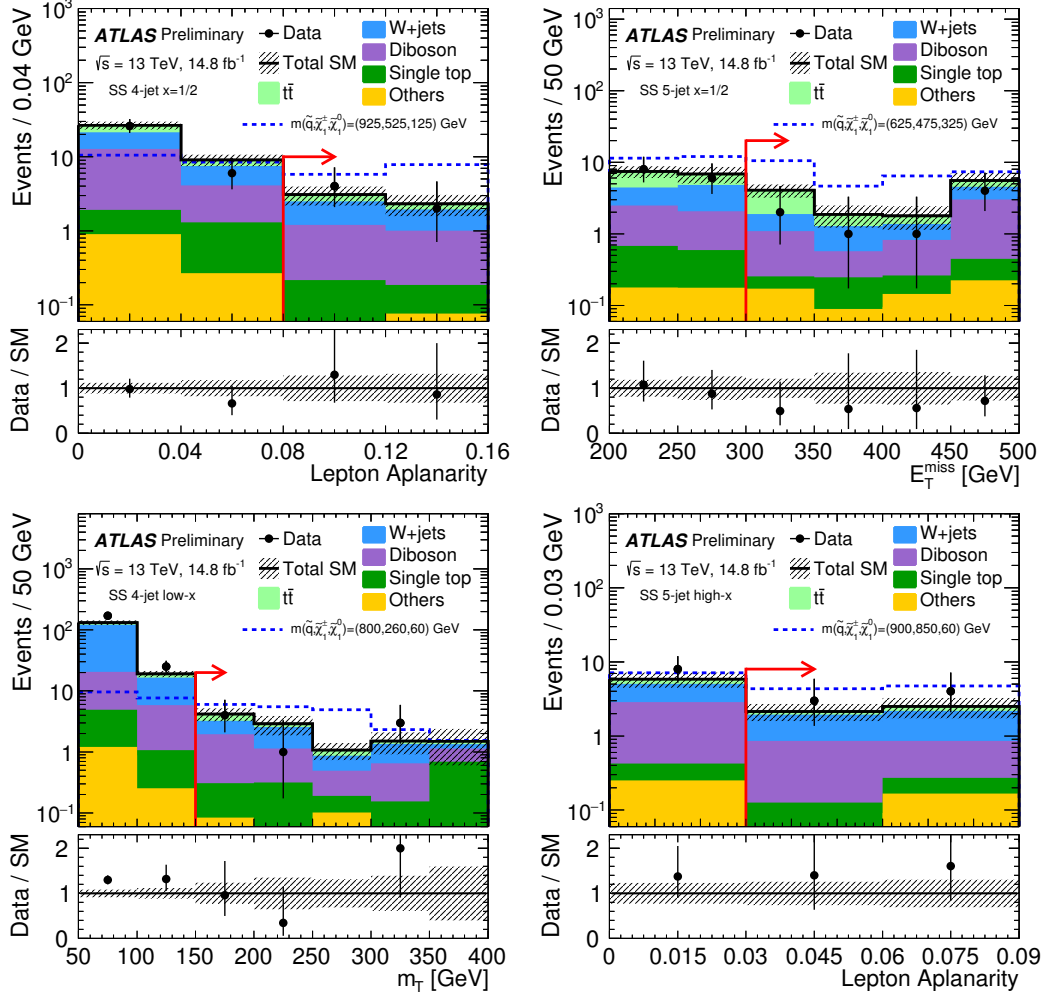
Figure 5: Distributions of the lepton aplanarity for the **SS 4J x=1/2** (top left) and the **SS 5J high-x** (bottom right) signal regions, of E_T^{miss} for the **SS 5J x=1/2** (top right) signal region and of m_T for the **SS 4J low-x** signal region (bottom left). The requirement on the variable plotted is removed from the definitions of the signal regions, where the arrow indicates the position of the cut in the signal region. The lower panels of the plots show the ratio of the observed data to the total background prediction as derived in the background-only fit. The uncertainty bands plotted include all statistical and systematic uncertainties as discussed in Section 7. The component 'Others' is the sum of Z+jets and $t\bar{t}$+V. The last bin includes the overflow.
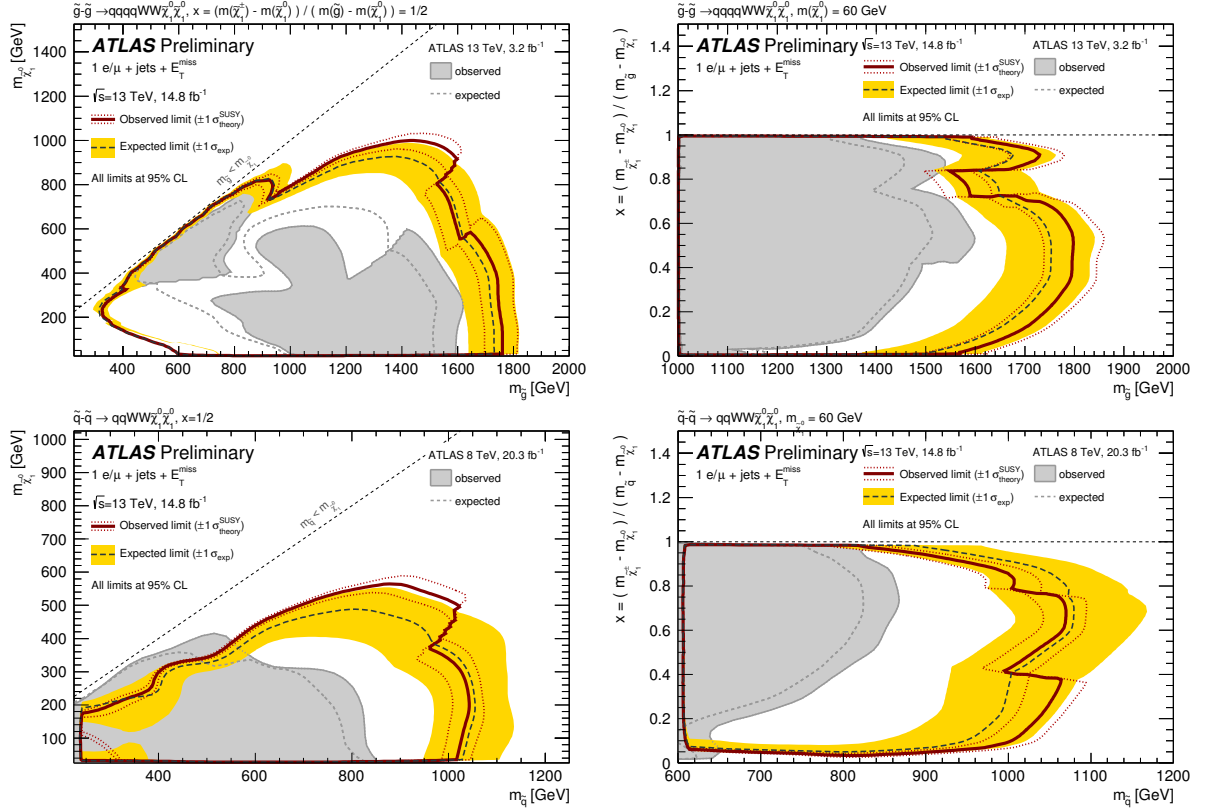
Figure 6: Combined 95% CL exclusion limits in the different SUSY models addressed by this analysis. In the top row, the two gluino models with different parametrisations are shown, with $m_{\tilde{g}}$ and $m_{\tilde{\chi}_1^0}$ floating (left) or $m_{\tilde{g}}$ and x floating (right). In the bottom row the two squark models are presented, with $m_{\tilde{q}}$ and $m_{\tilde{\chi}_1^0}$ floating (left) or $m_{\tilde{q}}$ and x floating (right). The red solid line corresponds to the observed limit with the red dotted lines indicating the $\pm 1\sigma$ variation of this limit due to the effect of theoretical scale and PDF uncertainties in the signal cross-section. The dark grey dashed line indicates the expected limit with the yellow band representing the $\pm 1\sigma$ variation of the median expected limit due to the experimental and theoretical uncertainties. The exclusion limits at 95% CL by previous ATLAS analyses [20, 21] are shown as the grey area.
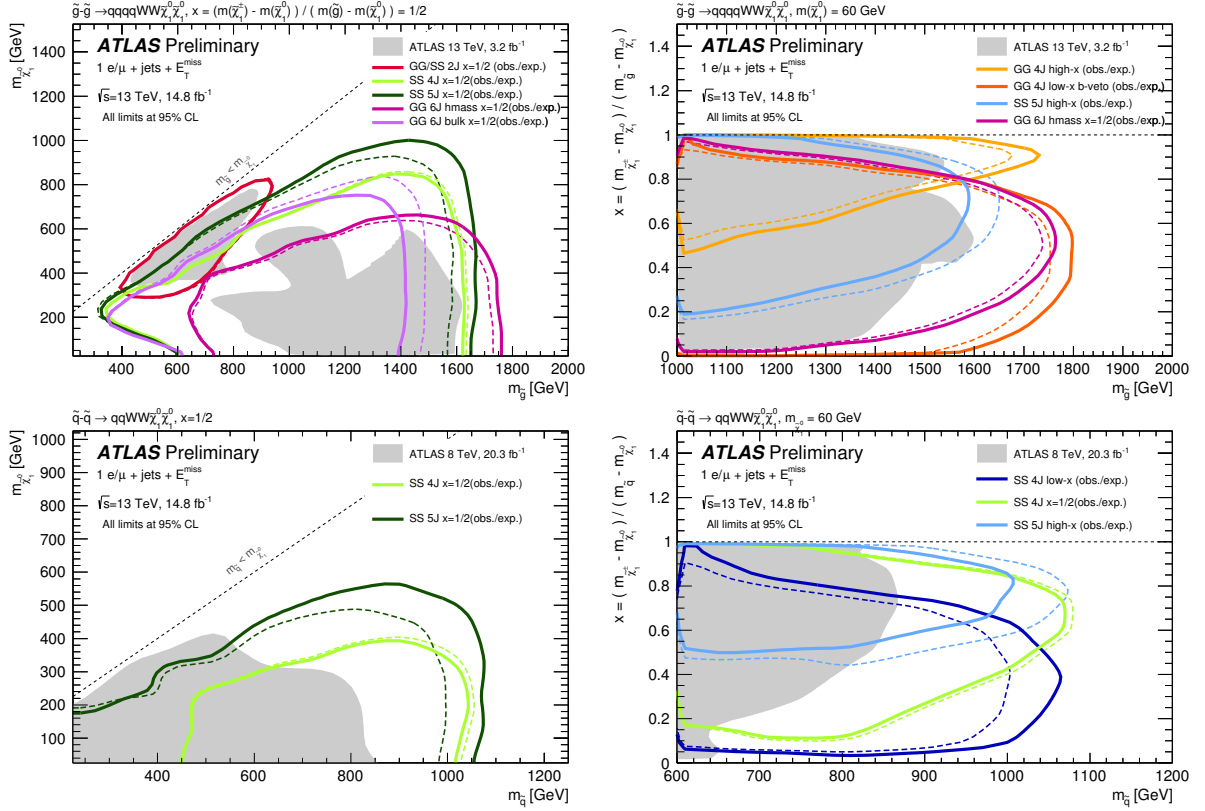
Figure 7: 95% CL exclusion limits for the individual signal regions in the models. Only signal regions resulting in the best expected limit are shown. The limit of **GG 6J bulk** is equally shown, as this signal region showed a small excess in the 2015 analysis [20]. In the top row, the two gluino models with different parametrisations are shown, with $m_{\tilde{g}}$ and $m_{\tilde{\chi}_1^0}$ floating (left) or $m_{\tilde{g}}$ and x floating (right). In the bottom row the two squark models are presented, with $m_{\tilde{q}}$ and $m_{\tilde{\chi}_1^0}$ floating (left) or $m_{\tilde{q}}$ and x floating (right). The dark grey dashed line indicates the expected limit with the yellow band representing the $\pm 1\sigma$ variation of the median expected limit due to the experimental and theoretical uncertainties. The exclusion limits at 95% CL by previous ATLAS analyses [20, 21] are shown as the grey area.

10 Conclusion

A search for squarks and gluinos in events with one isolated lepton, jets, and missing transverse momentum is presented. The analysis uses 14.8 fb^{-1} of proton–proton collision data at $\sqrt{s}$ = 13 TeV, collected by the ATLAS experiment at the LHC in 2015 and 2016. The search is performed in ten signal regions to provide sensitivity to a broad range of sparticle mass spectra for both squark- and gluino-pair production models.

The observed data agree with the Standard Model background prediction in the signal regions. For all signal regions, limits on the visible cross-section are derived in models of new physics within the kinematic requirements of this search. In addition, exclusion limits are placed on models with squark- or gluino-pair production and subsequent decays via an intermediate chargino to the lightest neutralino. Limits of previous searches conducted in LHC Run 1 are significantly extended. Gluino (squark) masses up to 1.8 TeV (1.1 TeV) are excluded for low neutralino masses ($\lesssim$ 400 GeV or $\lesssim$ 300 GeV) and chargino masses of $\sim$ 930 GeV (470 GeV or 650 GeV).

References

[1] Yu. A. Golfand and E. P. Likhtman,
    Extension of the Algebra of Poincare Group Generators and Violation of p Invariance,
    JETP Lett. **13** (1971) 323, [Pisma Zh. Eksp. Teor. Fiz.13,452(1971)].

[2] D. V. Volkov and V. P. Akulov, *Is the Neutrino a Goldstone Particle?*,
    Phys. Lett. B **46** (1973) 109.

[3] J. Wess and B. Zumino, *Supergauge Transformations in Four-Dimensions*,
    Nucl. Phys. B **70** (1974) 39.

[4] J. Wess and B. Zumino, *Supergauge Invariant Extension of Quantum Electrodynamics*,
    Nucl. Phys. B **78** (1974) 1.

[5] S. Ferrara and B. Zumino, *Supergauge Invariant Yang-Mills Theories*,
    Nucl. Phys. B **79** (1974) 413.

[6] A. Salam and J. A. Strathdee, *Supersymmetry and Nonabelian Gauges*,
    Phys. Lett. B **51** (1974) 353.

[7] P. Fayet, *Supersymmetry and Weak, Electromagnetic and Strong Interactions*,
    Phys. Lett. B **64** (1976) 159.

[8] P. Fayet, *Spontaneously Broken Supersymmetric Theories of Weak, Electromagnetic and Strong Interactions*, Phys. Lett. B **69** (1977) 489.

[9] N. Sakai, *Naturalness in Supersymmetric Guts*, Z. Phys. C **11** (1981) 153.

[10] S. Dimopoulos, S. Raby and F. Wilczek, *Supersymmetry and the Scale of Unification*,
     Phys. Rev. D **24** (1981) 1681.

[11] L. E. Ibañez and G. G. Ross, *Low-Energy Predictions in Supersymmetric Grand Unified Theories*,
     Phys. Lett. B **105** (1981) 439.

[12] S. Dimopoulos and H. Georgi, *Softly Broken Supersymmetry and SU(5)*,
     Nucl. Phys. B **193** (1981) 150.

[13] G. R. Farrar and P. Fayet, *Phenomenology of the Production, Decay, and Detection of New Hadronic States Associated with Supersymmetry*, Phys. Lett. B **76** (1978) 575.

[14] H. Goldberg, *Constraint on the Photino Mass from Cosmology*, Phys. Rev. Lett. **50** (1983) 1419, [Erratum: Phys. Rev. Lett.103,099905(2009)].

[15] J. R. Ellis et al., *Supersymmetric Relics from the Big Bang*, Nucl. Phys. B **238** (1984) 453.

[16] J. Alwall et al., *Searching for Directly Decaying Gluinos at the Tevatron*, Phys. Lett. B **666** (2008) 34, arXiv: 0803.0019 [hep-ph].

[17] J. Alwall, P. Schuster and N. Toro, *Simplified Models for a First Characterization of New Physics at the LHC*, Phys. Rev. D **79** (2009) 075020, arXiv: 0810.3921 [hep-ph].

[18] D. Alves et al., *Simplified Models for LHC New Physics Searches*, J. Phys. G: Nucl. Part. Phys. **39** (2012) 105005, arXiv: 1105.2838 [hep-ph].

[19] ATLAS Collaboration, *Search for squarks and gluinos in events with isolated leptons, jets and missing transverse momentum at $\sqrt{s}$ = 8 TeV with the ATLAS detector*, JHEP **04** (2015) 116, arXiv: 1501.03555 [hep-ex].

[20] ATLAS Collaboration, *Search for gluinos in events with an isolated lepton, jets and missing transverse momentum at $\sqrt{s}$ = 13 TeV with the ATLAS detector*, submitted to Eur. Phys. J. C (2016), arXiv: 1605.04285 [hep-ex].

[21] ATLAS Collaboration, *Summary of the searches for squarks and gluinos using $\sqrt{s}$ = 8 TeV pp collisions with the ATLAS experiment at the LHC*, JHEP **10** (2015) 054, arXiv: 1507.05525 [hep-ex].

[22] CMS Collaboration, *Search for new physics in events with same-sign dileptons and jets in pp collisions at $\sqrt{s}$ = 8 TeV*, JHEP **01** (2014) 163, [Erratum: JHEP01,014(2015)], arXiv: 1311.6736 [hep-ex].

[23] CMS Collaboration, *Search for new physics in the multijet and missing transverse momentum final state in proton-proton collisions at $\sqrt{s}$= 8 TeV*, JHEP **06** (2014) 055, arXiv: 1402.4770 [hep-ex].

[24] CMS Collaboration, *Search for supersymmetry in events with one lepton in proton-proton collisions at $\sqrt{s}$=13 TeV with the CMS experiment*, CMS-PAS-SUS-15-006 (2016), URL: https://cds.cern.ch/record/2140638.

[25] ATLAS Collaboration, *The ATLAS Experiment at the CERN Large Hadron Collider*, JINST **3** (2008) S08003.

[26] ATLAS Collaboration, *ATLAS Insertable B-Layer Technical Design Report*, ATLAS-TDR-19 (2010), URL: http://cds.cern.ch/record/1291633.

[27] ATLAS Collaboration, *Performance of the ATLAS Trigger System in 2010*, Eur. Phys. J. C **72** (2012) 1849, arXiv: 1110.1530 [hep-ex].

[28] J. Alwall et al., *The automated computation of tree-level and next-to-leading order differential cross sections, and their matching to parton shower simulations*, JHEP **07** (2014) 079, arXiv: 1405.0301 [hep-ph].

[29] T. Sjöstrand, S. Mrenna and P. Z. Skands, *A Brief Introduction to PYTHIA 8.1*, Comput.Phys.Commun. **178** (2008) 852, arXiv: 0710.3820 [hep-ph].

[30] L. Lönnblad and S. Prestel, *Matching Tree-Level Matrix Elements with Interleaved Showers*, JHEP **03** (2012) 019, arXiv: 1109.4829 [hep-ph].

[31] ATLAS Collaboration, *ATLAS Pythia 8 tunes to 7 TeV data*, ATL-PHYS-PUB-2014-021 (2014), URL: http://cdsweb.cern.ch/record/1966419.

[32] R. D. Ball et al., *Parton distributions with LHC data*, Nucl. Phys. B **867** (2013) 244, arXiv: 1207.1303 [hep-ph].

[33] D. J. Lange, *The EvtGen particle decay simulation package*, Nucl. Instrum. Meth. A **462** (2001) 152.

[34] W. Beenakker et al., *Squark and gluino production at hadron colliders*, Nucl. Phys. B **492** (1997) 51, arXiv: hep-ph/9610490.

[35] A. Kulesza and L. Motyka, *Threshold resummation for squark-antisquark and gluino-pair production at the LHC*, Phys. Rev. Lett. **102** (2009) 111802, arXiv: 0807.2405 [hep-ph].

[36] A. Kulesza and L. Motyka, *Soft gluon resummation for the production of gluino-gluino and squark-antisquark pairs at the LHC*, Phys. Rev. D **80** (2009) 095004, arXiv: 0905.4749 [hep-ph].

[37] W. Beenakker et al., *Soft-gluon resummation for squark and gluino hadroproduction*, JHEP **12** (2009) 041, arXiv: 0909.4418 [hep-ph].

[38] W. Beenakker et al., *Squark and gluino hadroproduction*, Int. J. Mod. Phys. A **26** (2011) 2637, arXiv: 1105.1110 [hep-ph].

[39] M. Krämer et al., *Supersymmetry production cross sections in pp collisions at $\sqrt{s}$ = 7 TeV*, CERN-PH-TH-2012-163 (2012), arXiv: 1206.2892 [hep-ph].

[40] C. Borschensky et al., *Squark and gluino production cross sections in pp collisions at $\sqrt{s}$ = 13, 14, 33 and 100 TeV*, Eur. Phys. J. C **74** (2014) 3174, arXiv: 1407.5066 [hep-ph].

[41] ATLAS Collaboration, *Simulation of top quark production for the ATLAS experiment at $\sqrt{s}$ = 13 TeV*, ATL-PHYS-PUB-2016-004 (2016), URL: http://cds.cern.ch/record/2120417.

[42] S. Alioli et al., *A general framework for implementing NLO calculations in shower Monte Carlo programs: the POWHEG BOX*, JHEP **06** (2010) 043, arXiv: 1002.2581 [hep-ph].

[43] H.-L. Lai et al., *New parton distributions for collider physics*, Phys. Rev. **D82** (2010) 074024, arXiv: 1007.2241 [hep-ph].

[44] P. Artoisenet et al., *Automatic spin-entangled decays of heavy resonances in Monte Carlo simulations*, JHEP **03** (2013) 015, arXiv: 1212.3460 [hep-ph].

[45] T. Sjöstrand, S. Mrenna and P. Z. Skands, *PYTHIA 6.4 Physics and Manual*, JHEP **05** (2006) 026, arXiv: hep-ph/0603175.

[46] J. Pumplin et al., *New generation of parton distributions with uncertainties from global QCD analysis*, JHEP **07** (2002) 012, arXiv: hep-ph/0201195.

[47] P. Z. Skands, *Tuning Monte Carlo Generators: The Perugia Tunes*, Phys. Rev. D **82** (2010) 074018, arXiv: 1005.3457 [hep-ph].

[48] M. Czakon and A. Mitov,
Top++: a program for the calculation of the top-pair cross-section at hadron colliders,
Comput.Phys.Commun. **185** (2014) 2930.

[49] N. Kidonakis,
Two-loop soft anomalous dimensions for single top quark associated production with a W- or H-,
Phys.Rev. D82 **D82** (2010) 054018, arXiv: 1005.4451 [hep-ph].

[50] P. Kant et al., *HATHOR for single top-quark production: Updated predictions and uncertainty estimates for single top-quark production in hadronic collisions*,
Comput. Phys. Commun. **191** (2015) 74, arXiv: 1406.4403 [hep-ph].

[51] ATLAS Collaboration, *Monte Carlo Generators for the Production of a W or Z/γ* Boson in Association with Jets at ATLAS in Run 2*, ATL-PHYS-PUB-2016-003 (2016),
URL: http://cds.cern.ch/record/2120133.

[52] T. Gleisberg et al., *Event generation with SHERPA 1.1*, JHEP **02** (2009) 007,
arXiv: 0811.4622 [hep-ph].

[53] T. Gleisberg and S. Höche, *Comix, a new matrix element generator*, JHEP **12** (2008) 039,
arXiv: 0808.3674 [hep-ph].

[54] F. Cascioli, P. Maierhofer and S. Pozzorini, *Scattering Amplitudes with Open Loops*,
Phys. Rev. Lett. **108** (2012) 111601, arXiv: 1111.5206 [hep-ph].

[55] S. Schumann and F. Krauss,
A Parton shower algorithm based on Catani-Seymour dipole factorisation, JHEP **03** (2008) 038,
arXiv: 0709.1027 [hep-ph].

[56] S. Höche et al., *QCD matrix elements + parton showers: The NLO case*, JHEP **04** (2013) 027,
arXiv: 1207.5030 [hep-ph].

[57] ATLAS Collaboration,
Single Boson and Diboson Production Cross Sections in pp Collisions at $\sqrt{s}$ = 7 TeV,
ATL-COM-PHYS-2010-695 (2010), URL: https://cds.cern.ch/record/1287902.

[58] ATLAS Collaboration, *Multi-Boson Simulation for 13 TeV ATLAS Analyses*,
ATL-PHYS-PUB-2016-002 (2016), URL: http://cds.cern.ch/record/2119986.

[59] ATLAS Collaboration,
Modelling of the t̄tH and t̄tV (V = W, Z) processes for $\sqrt{s}$ = 13 TeV ATLAS analyses,
ATL-PHYS-PUB-2016-005 (2016), URL: http://cds.cern.ch/record/2120826.

[60] A. Lazopoulos et al., *Next-to-leading order QCD corrections to t − t̄ − Z production at the LHC*,
Phys. Lett. B **666** (2008) 62, arXiv: 0804.2220 [hep-ph].

[61] J. M. Campbell and R. K. Ellis, *t̄t W production and decay at NLO*, JHEP **07** (2012) 052,
arXiv: 1204.5678 [hep-ph].

[62] ATLAS Collaboration, *The ATLAS Simulation Infrastructure*, Eur. Phys. J. C **70** (2010) 823,
arXiv: 1005.4568 [physics.ins-det].

[63] GEANT4 Collaboration, *GEANT4: A Simulation toolkit*, Nucl. Instrum. Meth. A **506** (2003) 250.

[64] ATLAS Collaboration,
The simulation principle and performance of the ATLAS fast calorimeter simulation FastCaloSim,
ATL-PHYS-PUB-2010-013 (2010), URL: http://cds.cern.ch/record/1300517.

[65] ATLAS Collaboration, *Summary of ATLAS Pythia 8 tunes*, ATL-PHYS-PUB-2012-003 (2012),
URL: http://cds.cern.ch/record/1474107.

[66] A. Sherstnev and R. Thorne, *Parton Distributions for LO Generators*,
Eur. Phys. J. C **55** (2008) 553, arXiv: 0711.2473 [hep-ph].

[67] ATLAS Collaboration, *Improved luminosity determination in pp collisions at $\sqrt{s}$ = 7 TeV using the ATLAS detector at the LHC*, Eur. Phys. J. C **73** (2013) 2518, arXiv: 1302.4393 [hep-ex].

[68] M. Cacciari, G. P. Salam and G. Soyez, *The Anti-k(t) jet clustering algorithm*,
JHEP **04** (2008) 063, arXiv: 0802.1189 [hep-ph].

[69] ATLAS Collaboration, *Properties of Jets and Inputs to Jet Reconstruction and Calibration with the ATLAS Detector Using Proton-Proton Collisions at $\sqrt{s}$ = 13 TeV*,
ATL-PHYS-PUB-2015-036 (2015), URL: http://cds.cern.ch/record/2044564.

[70] ATLAS Collaboration, *Jet Calibration and Systematic Uncertainties for Jets Reconstructed in the ATLAS Detector at $\sqrt{s}$ = 13 TeV*, ATL-PHYS-PUB-2015-015 (2015),
URL: http://cds.cern.ch/record/2037613.

[71] M. Cacciari and G. P. Salam, *Pileup subtraction using jet areas*,
Physics Letters B **659** (2008) 119 .

[72] ATLAS Collaboration, *Performance of pile-up mitigation techniques for jets in pp collisions at $\sqrt{s}$ = 8 TeV using the ATLAS detector*, (2015), arXiv: 1510.03823 [hep-ex].

[73] ATLAS Collaboration, *Tagging and suppression of pileup jets with the ATLAS detector*,
ATLAS-CONF-2014-018 (2014), URL: http://cds.cern.ch/record/1700870.

[74] ATLAS Collaboration, *Expected performance of the ATLAS b-tagging algorithms in Run-2*,
ATL-PHYS-PUB-2015-022 (2015), URL: http://cds.cern.ch/record/2037697.

[75] ATLAS Collaboration,
Commissioning of the ATLAS b-tagging algorithms using $t\bar{t}$ events in early Run-2 data,
ATL-PHYS-PUB-2015-039 (2015), URL: http://cds.cern.ch/record/2047871.

[76] ATLAS Collaboration,
Electron identification measurements in ATLAS using $\sqrt{s}$ = 13 TeV data with 50 ns bunch spacing,
ATL-PHYS-PUB-2015-041 (2015), URL: http://cds.cern.ch/record/2048202.

[77] ATLAS Collaboration, *Muon reconstruction performance in early $\sqrt{s}$ = 13 TeV data*,
ATL-PHYS-PUB-2015-037 (2015), URL: http://cds.cern.ch/record/2047831.

[78] ATLAS Collaboration, *Expected performance of missing transverse momentum reconstruction for the ATLAS detector at $\sqrt{s}$ = 13 TeV*, ATL-PHYS-PUB-2015-023 (2015),
URL: http://cds.cern.ch/record/2037700.

[79] ATLAS Collaboration, *Performance of missing transverse momentum reconstruction for the ATLAS detector in the first proton-proton collisions at at $\sqrt{s}$= 13 TeV*,
ATL-PHYS-PUB-2015-027 (2015), URL: http://cds.cern.ch/record/2037904.

[80] ATLAS Collaboration,
Selection of jets produced in 13 TeV proton-proton collisions with the ATLAS detector,
ATLAS-CONF-2015-029 (2015), URL: http://cds.cern.ch/record/2037702.

[81] C. Chen, *New approach to identifying boosted hadronically decaying particles using jet substructure in its center-of-mass frame*, Phys. Rev. D **85** (2012) 034007,
arXiv: 1112.2567 [hep-ph].

[82] ATLAS Collaboration, *Measurement of the muon reconstruction performance of the ATLAS detector using 2011 and 2012 LHC proton–proton collision data*, Eur. Phys. J. C **74** (2014) 3130, arXiv: 1407.3935 [hep-ex].

[83] M. Bahr et al., *Herwig++ Physics and Manual*, Eur. Phys. J. C **58** (2008) 639, arXiv: 0803.0883 [hep-ph].

[84] S. Frixione and B. R. Webber, *Matching NLO QCD computations and parton shower simulations*, JHEP **06** (2002) 029, arXiv: hep-ph/0204244.

[85] J. Alwall et al., *MadGraph 5 : Going Beyond*, JHEP **06** (2011) 128, arXiv: 1106.0522 [hep-ph].

[86] ATLAS Collaboration, *Measurement of W and Z Boson Production Cross Sections in pp Collisions at root $\sqrt{s}$ = 13 TeV in the ATLAS Detector*, ATLAS-CONF-2015-039 (2015), URL: http://cds.cern.ch/record/2045487.

[87] S. Frixione et al., *Single-top hadroproduction in association with a W boson*, JHEP **07** (2008) 029, arXiv: 0805.3067 [hep-ph].

[88] G. Cowan et al., *Asymptotic formulae for likelihood-based tests of new physics*, Eur. Phys. J. C **71** (2011) 1554, arXiv: 1007.1727 [physics.data-an].

[89] M. Baak et al., *HistFitter software framework for statistical data analysis*, Eur. Phys. J. C **75** (2015) 153, arXiv: 1410.1280 [hep-ex].

[90] A. L. Read, *Presentation of search results: The CL(s) technique*, J. Phys. G **28** (2002) 2693.